

Understanding And Applying Anisotropic Virus Particle Transport In Complex Media

by
Maxwell William Smith

A dissertation submitted to the Department of Chemical & Biomolecular
Engineering, Cullen College of Engineering in partial fulfillment of the requirements
for the degree of

Doctor of Philosophy
in Chemical Engineering

Chair of Committee: Dr. Jacinta C. Conrad

Co-Chair of Committee: Dr. Richard C. Willson

Committee Member: Dr. Patrick C. Cirino

Committee Member: Dr. Mehmet Orman

Committee Member: Dr. Jakoah Brgoch

Committee Member: Dr. Dmitri Litvinov

University of Houston
August 2021

Copyright 2021, Maxwell William Smith

Acknowledgements

For the guidance and support from my advisors Jaci and Dr. Willson over the course of my journey, for the great discussions and encouragement from my friends and colleagues, and for the faith and confidence of my family in my choices, I will always be grateful for all the people in my life who helped me push forward and affirm my own personal and professional strength.

Thank you.

Abstract

Advances in nanotechnology have improved medical diagnostics. For nanoparticle-based diagnostics, nanoparticle transport significantly impacts assay performance, especially for assays involving complex medical samples. Existing diffusion models for spherical nanoparticles are often used to predict transport in complex media, but the diffusion of anisotropic nanoparticles is not well understood.

Previous work in our group has demonstrated the effectiveness of highly-anisotropic filamentous viruses as diagnostic reporters. We studied the diffusion of filamentous viral nanoparticles in model polymer solutions using fluorescence microscopy and particle tracking analysis. The extracted virus dynamics were then compared with existing theories to determine which virus properties control virus diffusion. Our results indicate that virus anisotropy influences viral particle dynamics and enhances virus diffusion compared to spherical nanoparticles.

We also investigated the use of bacteriophage M13 in a reporter-exclusion immunoassay. We use the restricted-access adsorbent CaptoTM Core 700 to capture reporter molecule enzyme-antibody conjugate. By introducing M13 as a large binding scaffold, small protein hCG can be detected as the M13-analyte-reporter complex is excluded from the resin in the presence of analyte. Our results demonstrate the proof-of-concept and potential of this type of assay for a wide range of applications. Understanding the transport properties of filamentous viruses will be critical for fu-

ture development and implementation of virus-based diagnostics.

TABLE OF CONTENTS

| | |
|--|-------------|
| Acknowledgements | iii |
| Abstract | iv |
| Table of Contents | vi |
| List of Tables | viii |
| List of Figures | viii |
| 1 Virus Nanotechnology and Its Role in Medical Diagnostics | 1 |
| Nanotechnology Market and Research Trends | 1 |
| Nanoparticles and Nanotechnology | 4 |
| Nanoparticle Transport | 7 |
| Anisotropic Nanoparticles | 9 |
| Viruses and Nanotechnology | 10 |
| Application of Viruses in Diagnostic Settings | 12 |
| Viral Particles as Platform for Reporter Development | 14 |
| 2 Dynamics of Flexible Viruses in Polymer Solutions | 15 |
| Materials and Methods | 16 |
| Viral and spherical particles | 16 |
| PEG precipitation of PVM | 17 |
| Functionalization of virus particles | 17 |
| Preparation of virus-polymer solutions | 19 |
| Imaging and tracking of viruses | 19 |
| Results and Discussion | 21 |
| Viral nanoparticle dynamics | 21 |
| Scaling of the long-time diffusivity | 26 |
| Conclusions | 28 |
| 3 Isocratic Reporter-Exclusion Immunoassay Using Restricted-Access Adsorbents | 31 |
| Materials and Methods | 33 |
| Cultivation of M13 phage | 33 |
| Reporter-exclusion assay for M13 phage using restricted-access adsorbent | 33 |
| Immunochemical protein assay using restricted-access adsorbent | 34 |

| | |
|--|-----------|
| Results and Discussion | 35 |
| Reporter capture by restricted-access adsorbent | 35 |
| Isocratic detection of M13 phage using restricted access adsorbent . . | 36 |
| Isocratic reporter-exclusion immunodetection of small protein analytes | 36 |
| Conclusions | 39 |
| 4 Conclusions and Future Directions | 41 |
| Conclusions and Future Directions for Virus Dynamics | 41 |
| Conclusions and Future Directions for Size-Exclusion Assay | 45 |
| Bibliography | 50 |

LIST OF TABLES

| | | |
|---------|--|----|
| Table 1 | Different length scales S_i for PVM, M13, and pf1 virus particles. . | 27 |
|---------|--|----|

LIST OF FIGURES

| | | |
|-----------|---|----|
| Figure 1 | Nanotechnology research fields | 2 |
| Figure 2 | Global market value of nanomaterials | 3 |
| Figure 3 | Nanoscale material properties | 5 |
| Figure 4 | Dispersion of nanoparticles in porous medium | 7 |
| Figure 5 | Anisotropic gold nanoparticles | 9 |
| Figure 6 | Different virus shapes | 11 |
| Figure 7 | Sandwich ELISA schematic | 13 |
| Figure 8 | Virus particles and functionalization | 18 |
| Figure 9 | Viral particle mean squared displacement | 21 |
| Figure 10 | Viral particle normalized probability distribution of displacements | 23 |
| Figure 11 | Viral particle normalized probability distribution of displacements comparison | 24 |
| Figure 12 | Viral particle diffusivity versus normalized polymer concentration | 26 |
| Figure 13 | Viral particle normalized diffusivity versus normalized length scale | 29 |
| Figure 14 | Illustration of reporter-exclusion assay for large analytes such as viruses | 32 |
| Figure 15 | Flow-rate dependence of reporter capture in a reporter-exclusion assay for M13 virus particles | 36 |
| Figure 16 | Variation of reporter capture efficiency with phage concentration | 37 |
| Figure 17 | Schematic of small-analyte reporter-exclusion immunoassay using restricted-access adsorbent | 38 |
| Figure 18 | Detection of hCG using M13 phage anti-hCG conjugate as an ex- cluded capture carrier with HRP/Anti- β -hCG as reporter | 39 |

CHAPTER 1: Virus Nanotechnology and Its Role in Medical Diagnostics

In the healthcare sector, patient outcomes are often reliant on fast and accurate diagnosis, and advancements in diagnostic technology improve patient outcomes [1–5]. The field of nanotechnology was first posited by Dr. Richard Feynman in 1959 in the seminal talk “Plenty of Room at the Bottom.” In his talk, Dr. Feynman envisioned atomic-level control over materials where encyclopedias can be transcribed and read from an area as small as the head of the pin [6]. Since then, nanotechnology has become ubiquitous in our daily lives and will become only more prevalent as the field further develops. In the most general terms, nanotechnology is a technology based on materials with critical length scales in the 1-100 nm range [7]. This simple definition, however, understates the potential of this technology. As features become smaller, the microscopic properties of these systems differ greatly from the properties observed at the macroscopic scale, and effects that could have been assumed to be negligible become much more significant [8–11]. By utilizing these modified properties, nanotechnology can produce much more efficient systems than bulk materials, in a broad range of different applications.

Nanotechnology Market and Research Trends

Since the inception of the discipline, nanotechnology research has expanded in both scope and scale, with different application areas exploring different aspects of nanoscale properties and their potential applications [12–15]. The construction industry has developed many new nano-concrete formulations that improve their mechanical properties, and some can exhibit NO_x depollution effects [16, 17]. The food and agriculture sector has utilized nanotechnology in food production, like fertilizers and pesticides, and in food processing and packaging [18–21]. Nanotechnology has

also improved the energy sector with more efficient energy generation and energy storage materials [22–25]. More recently, there has been an increased focus on nanotechnology research from the chemical and medical perspectives. Nanotechnology is already having a substantial impact on the oil and gas and chemical engineering sectors. Nanofluids employed in oil and gas wells can have properties very different than pure water, including fluid viscosity and shearing, pore wettability, and hydrocarbon solubility. Nanocoatings have also improved equipment corrosion resistance to harsh effluent streams from the well [26–28]. New catalysts with nanoscale features can enhance reactivity and selectivity and reduce wasteful or harmful side products [29–31]. Improved synthesis techniques can produce advanced polymers for composite materials with stronger mechanical and even self-healing properties [32–34] and functionalization of surfaces and particles [35–37].

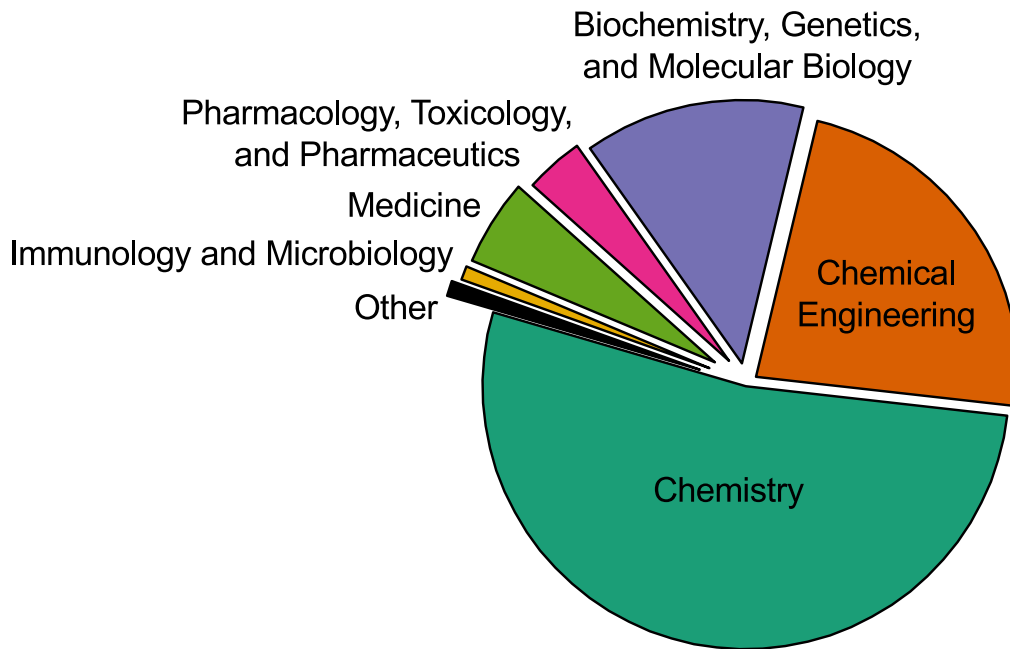


Figure 1: Distribution of nanotechnology-based research papers in chemistry and medicine. Adapted from [14].

There are many applications of nanotechnology in the healthcare sector as well. Antimicrobial and antifouling surfaces integrated into medical equipment can reduce device-associated infections, and bio-derived nanomaterials can limit immune

reactions to medical implants [38–42]. Drug molecules encapsulated by a coating material protect the payload from environment-induced inactivation and facilitate targeted delivery to desired areas for more effective drug action [15, 43–45]. Improved nanotechnology-based medical diagnostics increase sensitivity of detection of new biomarkers for existing and emerging diseases and allow the transition of some traditionally laboratory-based diagnostics to on-site point-of-care settings [46–49].

As research expands the range of potential applications, nanotechnology is already impacting global markets. Over the past ten years, the nanomaterials market value has increased from around \$1 billion to over \$10 billion. This trend is forecasted to continue over the next few years [50, 51].

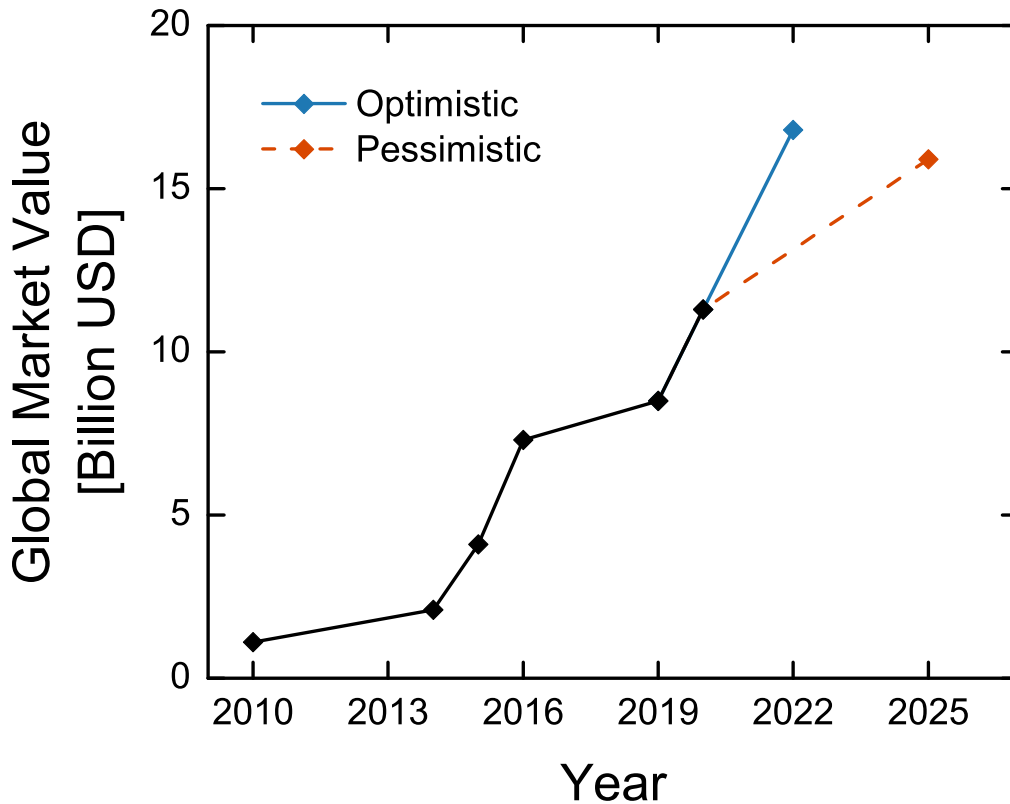


Figure 2: Estimated global market value of engineered nanomaterials, omitting liposomal drugs and vaccines, from 2010 to 2020 and pessimistic (orange) and optimistic (blue) projected market value. Adapted from [51].

This market trend is also reflected in nanotechnology research funding and patent filings since the beginning of the 21st century. In the early 2000s, government funding

for nanotechnology increased dramatically compared to the previous decade [12, 13]. Tens of thousands of patents were filed between 2001 and 2010, and by the 2010s, over 5,000 were filed each year globally [13, 15, 38, 50].

As nanotechnology becomes more widespread and recognizable, some public concerns also are coming to the forefront. Regulatory agencies are now examining nanoscale material environmental and health impacts more closely than in the past decades [52–55]. Regardless, nanotechnology will continue to be developed and integrated into more aspects of our lives.

Nanoparticles and Nanotechnology

Nanoparticles are often utilized in many nanotechnology applications. They are defined by having at least one dimension between 1 and 100 nm and can be manufactured from various materials. Nanoparticle synthesis is divided into two main categories, top-down and bottom-up [10]. The top-down approach involves using a bulk sample of the material and processing the sample into smaller structures. A typical top-down processing method is ball milling, which uses mechanical stress to break the bulk material into finer material [56, 57]. The bottom-up approach, in contrast, begins with smaller constituents such as atoms or molecules and assembles the components into the final structure. The bottom-up method is commonly used in industry due to the different possible synthesis routes for each nanoparticle type [10]. For inorganic nanoparticles, bottom-up synthesis techniques include chemical reduction and chemical precipitation of solubilized metal atoms or salts [56, 58, 59]. Polymer- and lipid-based nanoparticles are often fabricated using self-assembly processes. In aqueous self-assembly, hydrophobic interactions induce aggregation of the constituents to minimize unfavorable interactions and form nanoparticles with the nanoparticle size controlled by hydrophobic group packing and steric interactions [60–62]. Researchers are also exploring new synthesis techniques like bio-mediated

synthesis using plants [63], fungi [64], and viruses [65] and new processing methods like microwave shock [66].

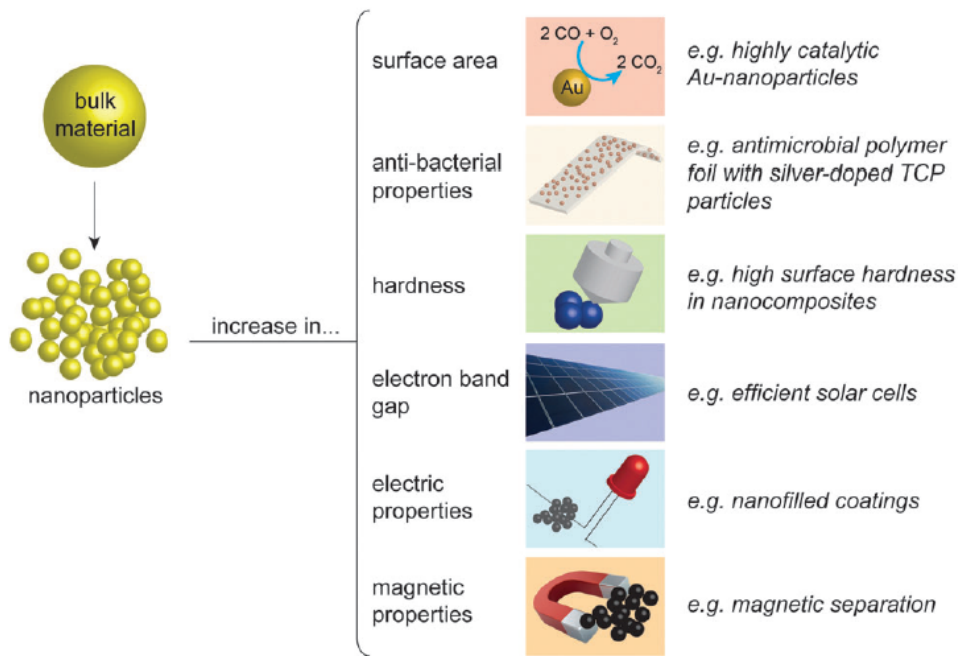


Figure 3: Different material property enhancements during the transition from macroscopic bulk material to nanoparticles [58].

Similar to other materials with nanoscale features, nanoparticles are distinguished by their diverging physical and chemical properties compared to larger particles of the same material. This divergence is directly related to the nanoparticle size. As particle size decreases, the surface area increases dramatically, scaling with the inverse of the particle size [8, 10, 67]. Higher surface area then influences other secondary properties. High surface areas enhance catalyst chemical reactivity during surface-mediated reactions due to more available atoms on faces and edges per volume of material [58, 68–70]. High surface area also equates to a larger interfacial area per volume, leading to stronger interactions between particles or between the particle and the surrounding environment [26, 71–73].

Smaller particles also exhibit altered electromagnetic properties due to quantum effects at these smaller sizes [8, 10]. Transition metal nanoparticles, like gold and sil-

ver, undergo surface plasmon resonance when excited by light which causes a strong extinction at specific wavelengths, controlled by the nanoparticle size [57, 74, 75]. Other metallic nanoparticles smaller than a critical length scale may display superparamagnetic properties with faster responses to imposed magnetic fields [76, 77]. Even elements that, in bulk, are usually nonmagnetic can become ferromagnetic when the particles are sufficiently small [57, 77, 78]. Semiconductor material also behaves differently at very small sizes. Quantum dots, made of semiconductor material, exhibit bright photoluminescence with an emission spectrum strongly dependent on the nanoparticle size [79, 80].

Nanoparticles can be functionalized with many different motifs that further tune the surface properties. Oligomers and polymers can either screen or promote interactions with other particles or the environment depending on the oligomer or polymer composition [81–83]. Inorganic shells can improve nanoparticle stability or change the mechanical, chemical, and electrical properties of the nanoparticle [77, 79, 84]. Nanoparticles functionalized with biomolecules allow targeting select biomarkers both *in vitro* and *in vivo* [85, 86].

These properties of nanoparticles have facilitated the use of nanoparticles in a large variety of applications across many different fields. For example, the surface-related properties are commonly utilized in catalysis [57, 58, 87], oil recovery [26–28], and material processing and manufacturing [58, 73, 81]. The electrical and optical properties, meanwhile, are utilized in consumer electronics [51, 67, 84], medical imaging [86], and diagnostics [74, 88, 89]. The success of these applications, however, also requires not only the physical properties of the nanoparticles alone. Nanoparticle transport through a medium significantly impacts an application’s final efficacy and must be considered along with the other nanoparticle properties.

Nanoparticle Transport

The chemistry of nanoparticles significantly impacts many different applications, but these properties are not the only factors that control the performance. Transport properties also affect performance. For example, nanoparticle drug carriers need to target only select areas of the patient to increase drug concentration in the targeted regions and decrease possible side-effects from unwanted interactions in other parts of the body [44, 75, 90]. In oil recovery, sedimentary rocks contain many pores of different sizes. Nanofluids need to move through these pores and maximize interactions between the nanoparticles and the oil on the pore surface to extract the oil [26–28, 91]. Nanocomposite materials require good nanoparticle dispersion through the material to achieve the mechanical reinforcement needed [17, 33, 81, 92]. In these applications, nanoparticles must transport through often dense and complex systems to provide the desired effect. Therefore, understanding and predicting nanoparticle transport is critical.

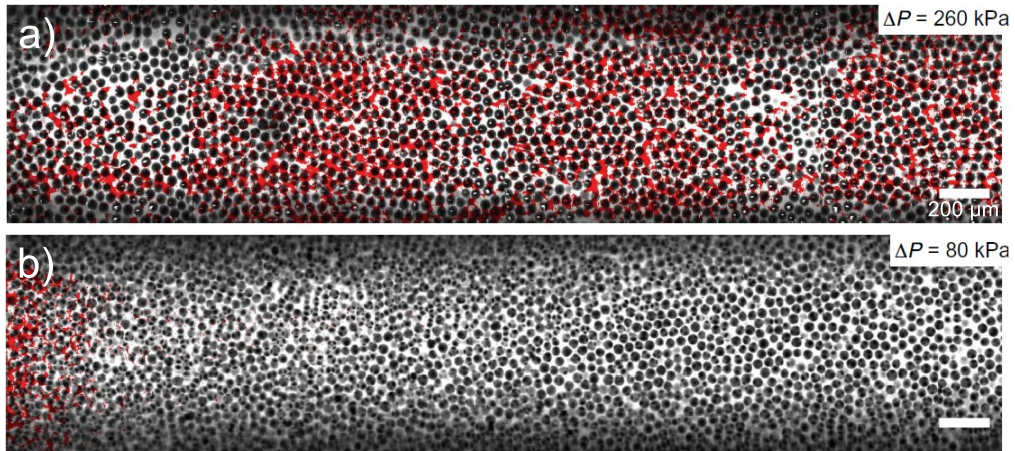


Figure 4: Confocal micrographs of 1 μm amine-functionalized polystyrene colloidal particles flowing left to right in packing of 38 - 45 μm glass beads with varying pressure drop. Scale bars represent 200 μm . Adapted from [93].

Transport of a component in any mixture is the combination of two terms, the convective motion and the diffusive motion. Convective motion, or flux, of a component is a function of the bulk motion, or flux, of the medium and velocity gradients in the

system. Convection is critical in systems where the velocity gradient is significantly affected by geometric constraints, i.e., small pores or changes in viscous stresses in space or time, i.e., polymeric medium. Process parameters, like volumetric flow and pressure, can be tuned to control convective transport. Diffusive transport, however, is not as readily controlled. Fick’s first law of diffusion describes the diffusive molar flux \mathbf{J}_i relative to the bulk motion,

$$\mathbf{J}_i = -D_i \nabla c_i \tag{1.1}$$

where D_i is the diffusion constant of component i in the mixture and ∇c_i is the concentration gradient of component i in the mixture [94]. On the nanoscale, the ∇c_i term does not vanish due to finite distance between individual particles and random thermal motion of the solute, i.e., Brownian motion. This detail means that diffusion must be accounted for in these nanoparticle-based nanotechnologies.

To predict the diffusivity D of a spherical particle in a fluid, a useful relation is the Stokes-Einstein (SE) equation,

$$D = \frac{k_B T}{6\pi\eta R} \tag{1.2}$$

where k_B is the Boltzmann constant, T is the temperature, η is the dynamic viscosity of the background fluid, and R is the particle radius. This relation was developed for homogenous fluid and fails to predict the particle diffusivity when the critical length scales of the particle and fluid are comparable. This situation is often present in the complex mixtures of many nanotechnology applications and can lead to substantial deviations from the SE prediction [95–97]. Several theories and models have been developed to account for these deviations. Obstruction models [98–100], hydrodynamic models [101–103], and coupling models [104–106] have demonstrated success when predicting deviations of nanoparticle diffusion in particular systems based on

the specific constraints. There are, however, issues with these models as they were developed within the framework of spherical particles with only one length scale, and many commonly used nanoparticles are anisotropic.

Anisotropic Nanoparticles

The classical diffusion models were developed to describe the diffusion of spherical, isotropic particles. Many nanotechnology applications, however, utilize anisotropic particles with simple shapes like rods and plates or with more complex geometries like nanostars and nanodendrites [107–109]. Anisotropic shapes can alter the inherent nanoparticle properties and their interactions with the surrounding environment and modify the behavior of the nanoparticle in these systems.

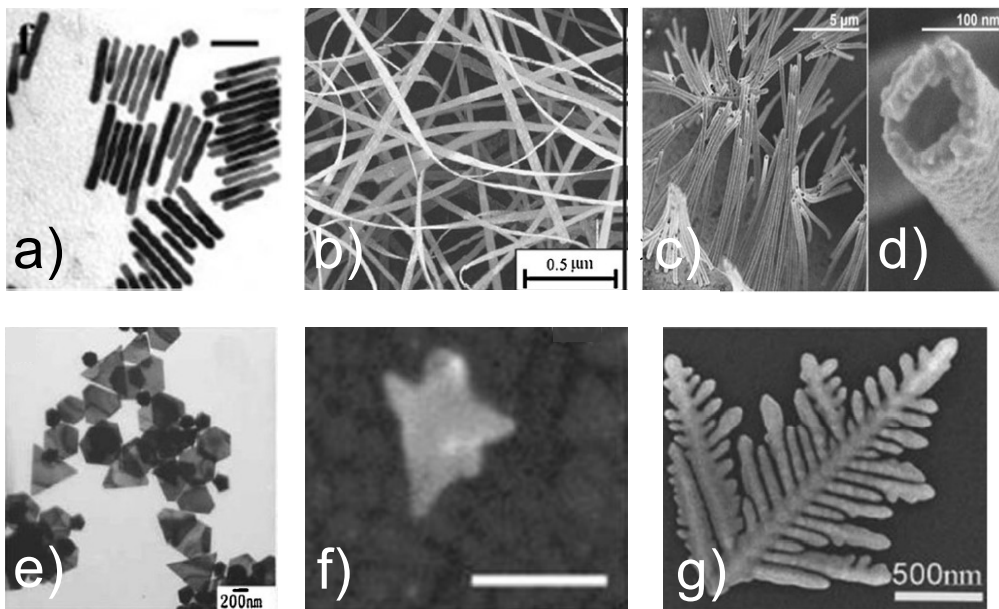


Figure 5: Examples of anisotropic gold nanoparticles with different shapes. Scale bars represent a) 50 nm, b) 0.5 μm , c) 5 μm , d) 100 nm, e) 200 nm, f) 100 nm, and g) 500 nm. Adapted from [108].

Anisotropic shapes increase the surface area per volume of nanoparticles, increasing the strength of the interactions between nanoparticles or with the environment. This surface area increase is often used to improve the mechanical strength of nanocomposites [110, 111]. The mechanical strength of anisotropic nanoparticles

themselves also varies between the different particle planes of symmetry and can contribute to the overall strength of the material [110, 112]. As discussed when comparing nanoparticles to bulk materials, nanoscale features can lead to new optical and electromagnetic properties. Shape anisotropies also produce a similar effect between anisotropic particles and spherical particles. For example, spectrum measurements of rod-like and plate-like gold nanoparticles show distinct absorption spectra with peaks shifted by hundreds of nanometers due to different plasmon resonance modes in different directions. The spectrum is further shifted within a shape by changing the size of the nanoparticle in different directions [107, 108, 113]. With the advantages of anisotropic nanoparticles for nanotechnology, understanding the effects of anisotropic shapes on the dynamics of these types of nanoparticles is critical.

Viruses and Nanotechnology

Viruses are organic nanoparticles that are found in nature. Since viruses were confirmed to be particles in the early 1900s [114, 115], over 6,500 individual virus species have been categorized [116], and over 220,000 complete viral genomes sequenced [117]. Some estimates indicate total viral diversity comprises millions of different virus species [118–120]. Despite their negative medical connotations, viruses as particles exhibit many inherent properties desirable for technological applications. These intrinsic properties result from the capsid protein chemistry and assembled structure controlled by the virus DNA/RNA. When a virus replicates, it infects a host cell with its viral DNA/RNA, and the host cell then produces the virus proteins. These proteins assemble into new virus particles, which are then released from the host cell to infect new cells.

The properties of a virus particle are a function of the viral DNA/RNA, the coat proteins, and the final assembled capsid structure. During viral replication, coat proteins assemble into a capsid around the DNA/RNA. This assembly process is driven

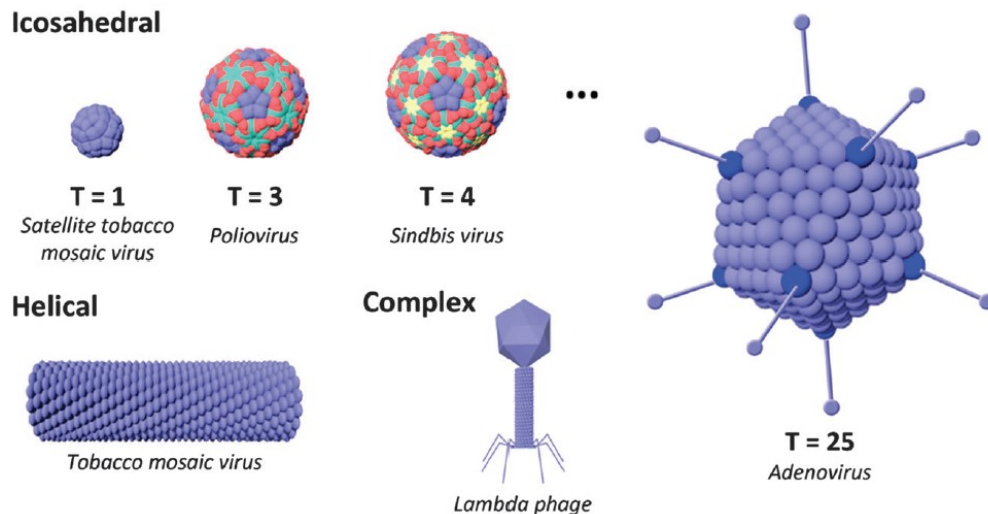


Figure 6: Examples of common virus shapes with example virus species in italics below virus schematic. Triangulation numbers (T) for icosahedral viruses show the effect of T on virus size and shape [121].

by interactions with the DNA/RNA and with other coat proteins. Surface chemistry and structure, in turn, are determined by the final assembled capsid structure. Protein residues displayed on the surface of the capsid control surface charge of the particle and possible interactions between the virus and other components of the system, i.e., surfaces, proteins, cells, etc [121–123]. The displayed residues can also be functionalized using different chemistries. The residues that contribute to protein-protein interactions control the structure, shape, and mechanical properties of the viral particle. With the large diversity of viruses, viral particles come in different shapes, from icosahedral [121–124] and helical symmetries [121–127] to more complex structures like head-to-tail particles [121, 123]. Virus size is generally controlled by the viral DNA/RNA length, which relates to how many coat protein copies are generated to package it. Since the virus genome controls the replication process, populations of viral particles are highly monodisperse. The regularity and controllability of virus replication are advantageous for many applications and expand the possibilities of virus application for existing and new nanotechnology [121, 128–131].

One such example of virus nanotechnology is phage display. It has already proven

to be an effective technique for screening protein binding affinities and selecting the desired binders such as antibodies from a mixture by modifying a population of a virus with randomized genes which display different peptides/proteins/antibodies on the virus surface, and selecting for binding [132, 133]. More recently, researchers are exploring the inherent properties of viruses and their use in other systems which previously relied on more traditional nanoparticles. For example, in medical applications, new vaccines and therapeutics have utilized virus particles to elicit immune responses by displaying specific peptides on the surface or transporting drug molecules to targeted areas [122, 134, 135]. Virus particles are also used as templating material. Biom mineralization of individual virus particles can create uniform nanostructures for use in electronics, catalysts, and nanocomposites [121, 127, 136–138]. Virus-based nanotechnology will continue to be integral to the future of the field as new and existing functionalization methods are developed.

Application of Viruses in Diagnostic Settings

Virus-based nanotechnology is also applied as a reporter platform in biomolecular and medical diagnostics, like diagnostic phage display and medical imaging [86, 121, 139]. As discussed previously, viruses display regular and controllable properties due to the nature of viral replication. This property affords virus particles a wide range of potential modifications and, therefore, applications in biomolecular detection and diagnostics [121, 139–142]. In general, effective biomolecular detection requires two principles, recognition and signaling. Recognition methods need to be selective for the targeted analyte. Common recognition methods include binding by specific antibodies or specific DNA or RNA sequences. Signaling processes need to generate a change in a known property before and after the recognition event. There are many possible signaling techniques, from light absorbance or emission to physical particle aggregation.

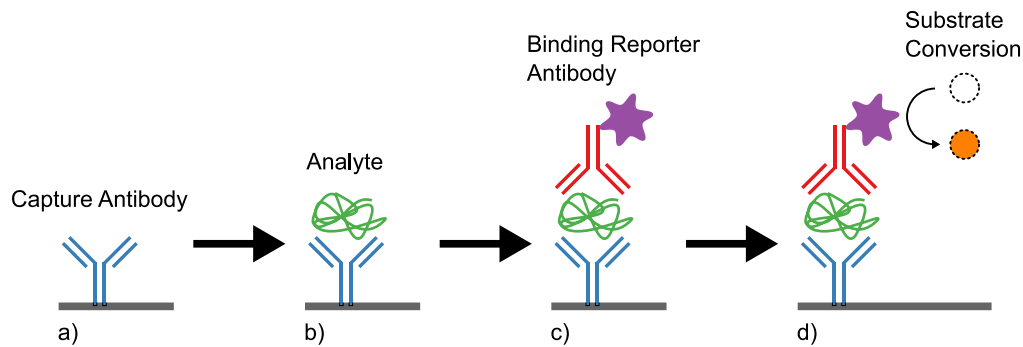


Figure 7: Schematic of sandwich ELISA. a) Capture antibody immobilized on surface. b) Analyte binds to capture antibody. c) Reporter binds to analyte-capture antibody complex. d) Enzyme converts substrate to produce signal.

An illustrative example of biomolecular detection is an enzyme-linked immunosorbent assay (ELISA) [143, 144]. In the sandwich format of this assay, a surface is functionalized with a capture antibody. When the analyte corresponding to the capture antibody is offered, the analyte binds to the capture antibody and is immobilized on the surface. Another antibody functionalized with a signal-generating enzyme called a reporter is then offered and binds to the capture antibody-analyte complex on the surface. The enzyme can then react with an offered substrate. In a negative test, i.e., when no analyte is offered, the reporter molecule does not bind and is washed away between reagent additions. The added substrate then does not react due to the absence of the enzyme. Conversely, in a positive test, i.e., analyte offered, the analyte bridges the immobilized capture antibody and the reporter molecule. In this case, the enzyme is still present when the substrate is added and catalyzes the substrate conversion into a detectable product. For this example, the reporter recognizes the analyte through antibody binding and signals through the conjugated enzyme.

For these biomolecular assays, reporter design can be different depending on the requirements of the assay. The main goal of each reporter, however, remains the same. Reporters need to recognize an analyte of interest and produce a measurable signal when the reporter recognizes the analyte [74, 80, 88, 145, 146]. Previous studies in our group have demonstrated the promise of filamentous viruses as medical assay

reporters [147–149].

Viral Particles as Platform for Reporter Development

Virus-based assays can leverage the virus binding affinity to their natural host cell for bacterial detection [140, 150–152], limiting the possible analytes a virus reporter can detect. By functionalizing the virus with different binding motifs, such as antibodies, a variety of biomolecules can be detected by virus reporters for other assay formats [153–157]. Previous studies in our group have also utilized filamentous M13 bacteriophage (phage) reporters to develop immunoassays to detect proteins and virus-like particle models with much better sensitivity than commercial gold nanoparticles [147–149, 158]. Furthermore, phage shape and, by extension, particle orientation affect reporter binding in lateral flow assays (LFA) [159, 160]. These studies were performed in buffer solutions, however, and while some assays utilize extensive pre-assay sample preparation, many samples of interest are complex mixtures of proteins, polysaccharides, cells, etc. As discussed earlier, complex mixtures impact diffusive transport of nanoparticles, and anisotropic nanoparticles diffuse differently in these systems than isotropic particles [124, 161].

Here we explore the dynamics of filamentous viral particles in semidilute polymer solutions using fluorescence microscopy and particle tracking algorithms. We then correlate the dynamics with particle diffusion to understand the critical length scales of these viruses and the length scale impact on virus diffusion. With this methodology, diffusion of filamentous viruses can be predicted and possibly extended to any filamentous particle for different nanotechnologies beyond virus-based assays.

CHAPTER 2: Dynamics of Flexible Viruses in Polymer Solutions

Highly anisotropic nanoparticles are used to impart desired functionality to polymer nanocomposites[162, 163], to deliver drugs and therapeutic agents in nanomedicine[164], and as nanoscale viscometers in complex fluids [165]. The transport of anisotropic particles in polymer solutions and melts, essential for these applications, is expected to differ from that of micron-size spherical particles. For spherical nanoparticles, the Stokes-Einstein (SE) equation $D_{SE} = k_B T / 6\pi\eta R_{NP}$ relates the diffusion coefficient D_{SE} of a particle of radius R to the viscosity η of the background fluid, which is assumed to be homogeneous. The assumption that a complex fluid is homogeneous is not valid, however, when the length scales of the particle and the fluid are comparable, as is often found for nanoparticles in polymer media. Thus, the diffusivity of nanoparticles in polymer solutions and melts can strongly deviate from the SE prediction [95–97, 103, 166]. Several theories and models have been developed to describe nanoparticle dynamics in polymeric matrices. In obstruction models, polymer coils are treated as static and rigid objects around which the particle must move [98–100]. Hydrodynamic models, alternatively, posit that polymers interact with particles through viscous drag and predict that hydrodynamic interactions are screened over the polymer correlation length ξ [101–103]. Scaling models extend hydrodynamic theories to account for coupling between the particle dynamics and those of the surrounding polymer chains [104–106].

These theories, however, were developed for isotropic, spherical nanoparticles and may not be readily applicable to anisotropic particles, which are characterized by multiple length scales [165, 167]. Even in Newtonian fluids, nanorods experience different viscous forces and angular moments than nanospheres of equal radius [168–171]. In polymer systems, nanorods with aspect ratios $AR = L/R$ of order 10 violate Stokes-

Einstein predictions to diffuse faster than spherical particles of similar hydrodynamic radius when the nanorod diameter $2R$ is comparable to characteristic polymer length scales [124, 172–174]. Further, as AR increases, the nanorod translational diffusivity D_t decreases more slowly than rotational diffusivity D_r [174, 175]. Tuning the interactions between the nanorod and the polymer matrix can also increase the diffusivity of nanorods [161]. While these comparisons have provided important insights into how to tune diffusion, how anisotropic particles experience local structural heterogeneities remains incompletely understood. Intriguingly, the fact that the enhanced diffusivity of nanorods diminishes as L/R is increased [161, 174] suggests that a competition between L and R controls nanorod diffusion.

Here, we measure the dynamics of semiflexible, anisotropic virus particles as model nanorods with large aspect ratios in semidilute polymer solutions. Using fluorescence microscopy, we quantify the dynamics of three labeled filamentous viruses, PVM, M13, and pf1, in solutions of partially hydrolyzed polyacrylamide. The long-time diffusion coefficients of the filamentous viral nanoparticles are an order of magnitude faster than expected but do not collapse onto a universal curve based on existing models for rods [168–170, 176] or spheres [105]. Instead, the long-time diffusion coefficients can be collapsed onto a master curve as a function of the ratio of the polymer correlation length ξ and a length scale between virus L and R . This collapse demonstrates the important role of particle length scales on the dynamics of highly anisotropic viral nanoparticles in polymer solutions.

Materials and Methods

Viral and spherical particles

Three different filamentous viral nanoparticles were used in these experiments: a plant virus, Potato virus M (PVM; ASLA biotech), and two filamentous bacteriophage (viruses that infect bacteria), M13 (Guild Biosciences), and pf1 (ASLA biotech)

(Figure 8(a)) [160]. M13 [177] and pf1 [178] are semiflexible viruses whose persistence length $L_p \cong 2 \mu\text{m}$ is comparable to their contour length $L = 900 \text{ nm}$ and $2 \mu\text{m}$, respectively. Although the persistence length for PVM has not been reported, the viral coat protein assembly of PVM [179] is similar to that of M13 and pf1. Therefore, we hypothesize that the L_p of PVM is comparable to that of M13 and pf1. The ratio $L_p/L \cong 0.1$ for PVM ($L = 200 \text{ nm}$) suggests that PVM behaves as a rigid rod. Three spherical fluorescent polystyrene particles of diameter 100 nm, 300 nm, and $2 \mu\text{m}$ (Fluoro-Max Red Aqueous Fluorescent Particles, excitation and emission wavelengths of 542 and 612 nm respectively; Thermo Fisher Scientific) were used as control particles.

PEG precipitation of PVM

To increase the PVM concentration in the stock solutions prior to functionalization, PVM particles were precipitated using a 20% w/v solution of poly(ethylene glycol) (PEG, weight average molecular weight $7450 \times \text{g mol}^{-1}$; Spectrum Chemical Manufacturing Corp.) in 2.5 M sodium chloride solution at a volume ratio of 1 part PEG solution to 5 parts stock PVM solution. The PVM/polymer solution was incubated with PEG for 1 hour at $4 \text{ }^\circ\text{C}$ and then centrifuged for 30 min at 3200 g, after which the virus particles were re-suspended in 1x PBS (1x phosphate-buffered saline solution). Because stock concentrations of M13 and pf1 were sufficiently high, these samples did not require concentration prior to functionalization.

Functionalization of virus particles

Viruses were labeled with the fluorescent dye Alexa555 (Alexa Fluor 555 NHS Ester, excitation and emission wavelengths of 488 nm and 532 nm respectively; Thermo Fisher Scientific). The N-hydroxysuccinimide (NHS) group covalently bonds to the primary amines of the coat protein's N-terminus (Figure 8(b)) [159]. The virus stock (100 μL) was buffer exchanged from the storage buffer to the dye conjugation buffer,

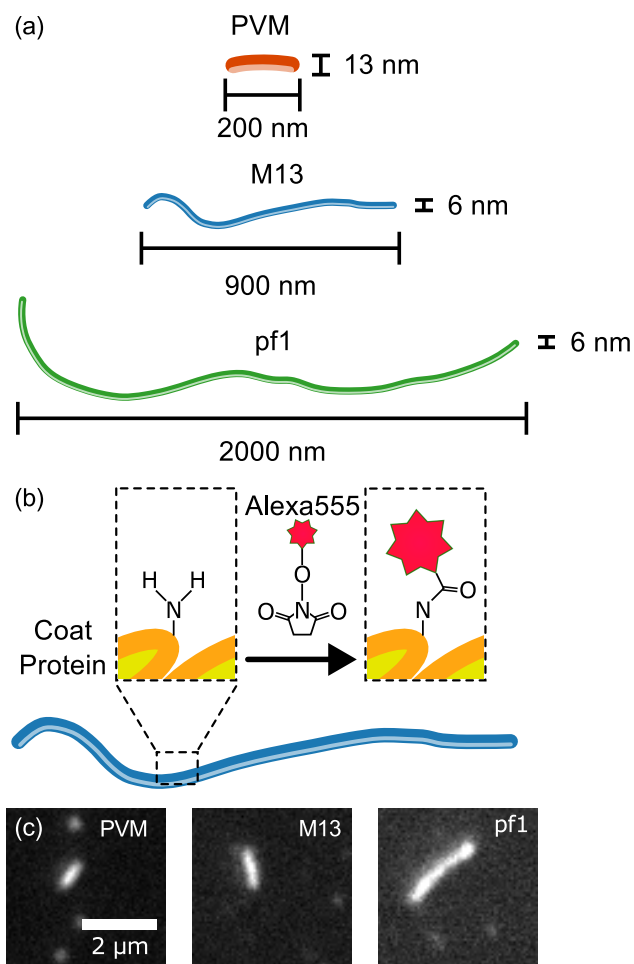


Figure 8: (a) Schematics of PVM, M13, and pf1 viruses. (b) Fluorescence labelling of the virus coat proteins with Alexa555. (c) Fluorescence micrographs of fluorescently labelled virus particles on glass slide surface.

0.2 M sodium bicarbonate at pH 8.3, using a Zeba column (Zeba Spin Desalting Column, 7K MWCO; Thermo Fisher Scientific). After buffer exchange, 10 μ L of Alexa555 dye solution (10 mg/mL Alexa555 in dimethyl sulfoxide; Thermo Fisher Scientific), was added to the buffer-exchanged virus solution and incubated overnight at 4 °C. The virus-dye solutions were dialyzed with a Float-A-Lyzer (Float-A-Lyzer Dialysis Device; Spectrum Laboratories Inc.) to remove any unreacted dye. Solutions containing M13 and pf1 were dialyzed with a 1 mL, 100 kD MWCO Float-A-Lyzer. Solutions containing PVM, the smallest virus, were first PEG precipitated, resuspended in 1x PBS, and then dialyzed using a 1 mL, 3.5 – 5 kD MWCO Float-A-Lyzer. The dialysis

buffer volume (1 L) was changed after 2 hours for three cycles at room temperature and then overnight at room temperature. After dialysis, dyed virus particles were imaged using fluorescence microscopy to confirm the success of the dyeing protocol.

Preparation of virus-polymer solutions

Partially hydrolyzed polyacrylamide (HPAM, FLOPAAM 3330; SNF) was used as a model crowding agent. To determine the overlap concentration, the viscosity as a function of HPAM concentration in 1x PBS was measured using an Ubbelohde viscometer (Supporting Information). The intrinsic viscosity $[\eta] = 3.2 \text{ L g}^{-1}$ was extracted from the first-order pseudo-virial expansion of viscosity η as a function of polymer mass concentration c , $\eta = \eta_0(1 + [\eta]c)$. The overlap concentration $c^* = 0.31 \text{ g L}^{-1}$ was estimated as the inverse of the intrinsic viscosity $c^* = 1/[\eta]$. The radius of gyration $R_g = 220 \text{ nm}$ of the HPAM in 1x PBS was then calculated by

$$R_{g,0} = \left(\frac{M_w}{\frac{4}{3}\pi N_{av}[\eta]} \right)^{1/3} \quad (2.1)$$

where $M_w = 8 \times 10^6 \text{ g mol}^{-1}$ is the molecular weight of HPAM, and N_{av} is Avogadro's number. Homogeneous HPAM/PBS stock solutions were prepared by mixing HPAM in 1x PBS at a concentration of 18.6 mg mL^{-1} using a tube roller for 1 week at room temperature to create a $60c^*$ stock solution. Polymer solutions were prepared by diluting the homogenized stock solution to the desired concentration. Virus particles were added to the homogenized polymer solutions and allowed to equilibrate overnight at 4°C .

Imaging and tracking of viruses

Viral nanoparticles were imaged in air-tight sample chambers consisting of glass microscope slides (Gold Seal Cover Glass; Thermo Fisher Scientific) that were sealed with Norland Optical Adhesive 81 (Norland Products). To reduce non-specific bind-

ing of viruses on the surface of the sample chambers, microscope slides were coated with BSA (bovine serum albumin heat shock fraction, pH 7, $\geq 98\%$; Thermo Fisher Scientific) prior to chamber assembly. Slides were soaked in a solution of 2.5% w/v BSA in water for 1 hour at room temperature. After soaking, the slides were wiped carefully with Kimwipes to remove excess liquid and dried, covered, overnight at room temperature.

Viral nanoparticles suspended in polymer solutions were imaged on a DMI3000 B microscope (Leica) furnished with an HCX PL APO 100x/1.40-0.70 oil immersion objective (Leica) and an N2.1 filter cube (Leica) using a sCMOS pco.edge 4.2 m camera (PCOTM) at 20 frames per second and 50 ms exposure time. The focus of the objective lens was positioned at least 20 μm away from the bottom surface of the sample chamber to minimize any effects from the chamber surfaces. Five microscope videos with 1000 frames per video were captured and analyzed using particle-tracking algorithms [180] to obtain particle trajectories. Although the virus dimensions cannot be directly extracted from microscopy because the virus nanoparticle diameter is below the optical diffraction limit, the centroids of the viruses can still be imaged and tracked over time.

From the particle trajectories, the one-dimensional, ensemble-averaged mean-squared displacement (MSD) $\langle \Delta x^2 \rangle$ was calculated as a function of lag time Δt . For each polymer solution concentration, D_t was extracted from a linear fit of the long-time MSD versus lag time via $\langle \Delta x^2 \rangle(\Delta t) = 2D_t \Delta t$. We also calculated the probability distribution of displacements (PDD) $G_s(\Delta x, \Delta t) = \frac{1}{N} \left\langle \sum_{i=1}^N \delta(x_i(t) - x_i(t + \Delta t) - \Delta x) \right\rangle$ [180], which measures the probability of a particle displacing a distance Δx at a lag time Δt .

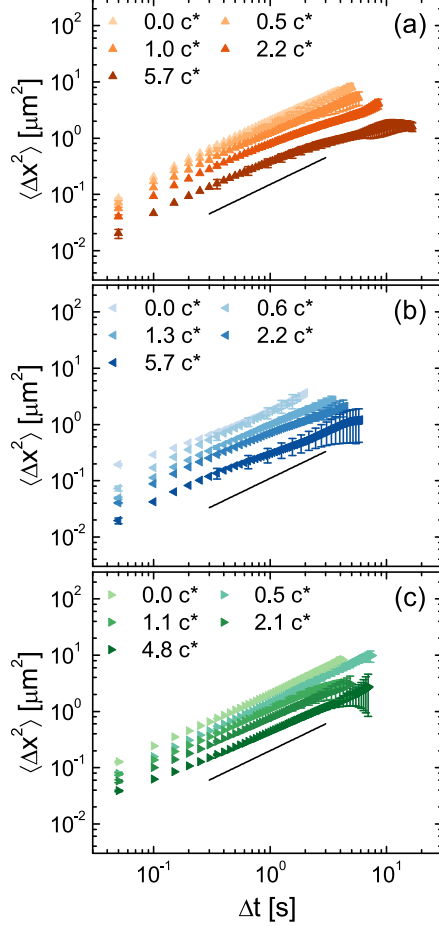


Figure 9: Mean squared displacement $\langle \Delta x^2 \rangle$ as a function of lag time Δt for virus particles (a) PVM, (b) M13, and (c) pf1 at various polymer concentrations c/c^* . Solid reference lines represent linear scaling.

Results and Discussion

Viral nanoparticle dynamics

We first examine the diffusivity of viral nanoparticles in the absence of polymer. The MSDs of PVM (aspect ratio AR of 15), M13 (AR of 150), and pf1 (AR of 330) suspended in 1x PBS scale approximately linearly with Δt . From a linear fit of the MSDs, we determine the translational diffusivities D_0 as $1.63 \pm 0.07 \mu\text{m}^2 \text{s}^{-1}$, $1.57 \pm 0.12 \mu\text{m}^2 \text{s}^{-1}$, and $2.02 \pm 0.14 \mu\text{m}^2 \text{s}^{-1}$ for PVM, M13, and pf1, respectively. The corresponding hydrodynamic radii, determined using the SE equation, are $131 \pm 6 \text{ nm}$, $136 \pm 11 \text{ nm}$, and $106 \pm 8 \text{ nm}$ for PVM, M13, and pf1, respectively. The

diffusivity measured for M13 in dilute solution is in reasonable agreement with earlier measurements of the diffusivity of another Ff bacteriophage, the closely-related and structurally-similar *fd* virus [181, 182], and is somewhat larger than the diffusivity of M13 in concentrated solutions near the isotropic-to-nematic transition [183]. The hydrodynamic radii of M13 and pf1 are much smaller than the radius of gyration of rigid rods of corresponding length and width (520 nm and 1200 nm, respectively, for M13 and pf1), suggesting that these viruses behave as semiflexible particles. This observation is consistent with expectations based on the ratio of virus persistence length L_p and contour length L , which for M13 and pf1 are 0.45 and 1.0, respectively [177, 178]. The measured hydrodynamic radius of PVM, however, is close to that of its rigid-rod counterpart (120 nm), consistent with $L_p/L = 0.1$.

The MSDs of PVM, M13, and pf1 scale approximately linearly with Δt for all c/c^* within the experimental error. This linearity indicates that the viral nanoparticles move diffusively through the polymer solution on all accessible time scales (Figure 9). Similar diffusive behavior has been observed for other anisotropic nanoparticles, including colloidal nanorods diffusing through polymeric [161] and mucosal gels [184], entangled wormlike micelle solutions [185], and semidilute and entangled polymer solutions [172]. Likewise, the MSDs of spherical particles scale linearly with Δt on accessible time scales (Supporting Information). Additionally, the virus MSDs decrease with increasing c/c^* as the viscosity of the polymer solutions increases. The MSDs represent an ensemble average of the particle dynamics, but do not provide information on how individual particles move through the solutions. Thus, to elucidate the microscopic processes that control viral nanoparticle transport, we next examine the distributions of particle displacements.

Even though the virus MSDs increase linearly with time, the PDDs $G_s(\Delta x, \Delta t)$ are strongly non-Gaussian for all three viral nanoparticles (PVM, M13, pf1) and for all polymer concentrations (Figure 10). To compare the dynamics of particles at differ-

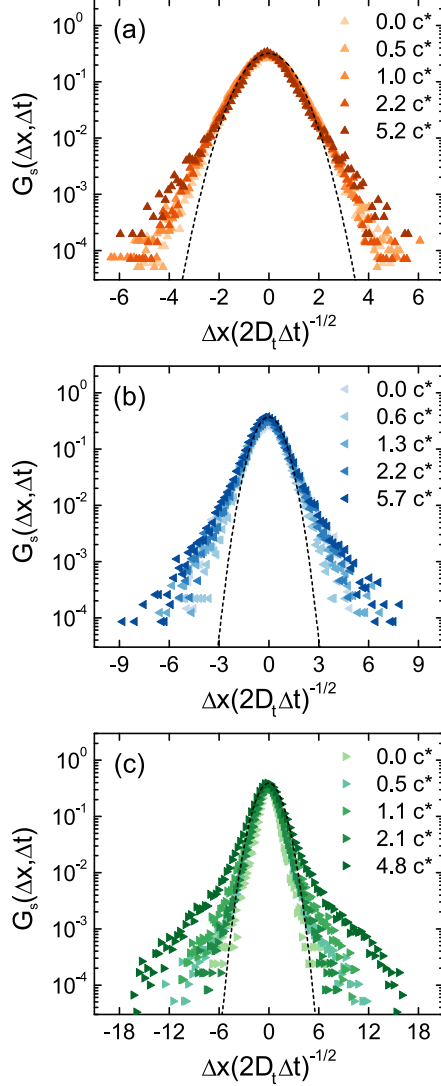


Figure 10: Probability distribution of displacements $G_s(\Delta x, \Delta t)$ as a function of displacement $\Delta x(2D_t\Delta t)^{-1/2}$ for virus particles (a) PVM, (b) M13, and (c) pf1 at $\Delta t = 0.05$ s at various polymer concentrations c/c^* . The dashed line indicates a Gaussian distribution.

ent c/c^* , we normalize displacement Δx by the diffusive displacement at lag time Δt , $(2D_t\Delta t)^{1/2}$. For a given virus, the extended tails of the PDDs more strongly deviate from the Gaussian prediction as c/c^* is increased. Both the maximum displacement and the probability of large displacements increase with polymer concentration. Similarly, for a constant c/c^* the non-Gaussianity of the PDDs is enhanced as the virus AR is increased (PVM < M13 < pf1). These two effects result in smaller deviations from

the Gaussian distribution for PVM and larger deviations for pf1 (Figure 11). Thus, these viral nanoparticles exhibit Fickian but non-Gaussian dynamics [186] in semidilute polymer solutions. These dynamics may arise from one or more mechanisms. The displacement distributions include contributions from motions both parallel to and perpendicular to the long axis of the phage. The relative contributions likely change as the phage aspect ratio is increased, and as the medium response becomes increasingly non-Newtonian (i.e. as the polymer concentration is increased). Additionally, non-Gaussian PDDs are reported for shapes in which the center of hydrodynamic stress does not coincide with the center of tracking [187, 188]. This effect may also contribute to the pronounced non-Gaussian PDDs of the semiflexible M13 and pf1.

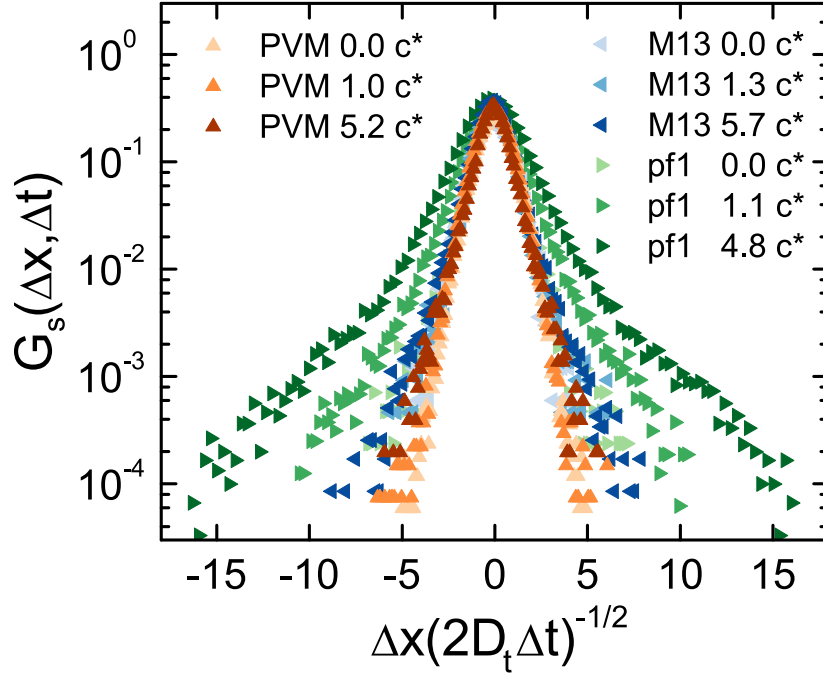


Figure 11: Comparison of virus $G_s(\Delta x, \Delta t)$ as a function of $\Delta x(2D_t\Delta t)^{-1/2}$ for virus particles PVM, M13, and pf1 at polymer concentrations c/c^* below and above the overlap concentration c^* .

Fickian diffusion concurrent with non-Gaussian displacement distributions have been widely reported for particles in complex fluids [189–193]. This behavior is often attributed to a distribution of diffusivities [23, 186, 189], which can arise as particles experience distinct local environments due to structural heterogeneities; through spa-

tial and temporal variations in hydrodynamic interactions through the medium; or through the formation and breaking of transient cages, leading to activated hopping [105, 106, 185, 194–196]. To assess the importance of structural heterogeneities for non-Gaussian dynamics, we calculated the PDDs for spherical particles of comparable hydrodynamic radii in the polymer solutions. The PDDs collapse onto a single Gaussian distribution for all spherical particles and for all c/c^* (Supporting Information). This result is consistent with earlier studies of spherical particles in semidilute polymer solutions [193, 197, 198] and suggests that structural heterogeneities in the solution do not control the non-Gaussian dynamics exhibited by the viruses. The solutions are formulated at concentrations below the entanglement concentration of HPAM in 1x PBM ($c_E > 20c^*$, Supporting Information), indicating that entanglements do not contribute to the non-Gaussian dynamics. Similarly, neither reptation [199–201] nor hopping mechanisms can explain viral nanoparticle dynamics in solutions of concentration less than c_E .

Instead, we hypothesize that the anisotropy of filamentous viruses gives rise to the non-Gaussian distributions observed for virus dynamics. Filamentous viruses are characterized by two length scales – their radius R and width L . We posit that the two characteristic length scales result in different degrees of coupling between viral nanoparticle dynamics and those of the polymer in solution when the virus displaces parallel or perpendicular to its major axis. Differences in the hydrodynamic drag forces acting on each of these modes then leads to a distribution of diffusivities. In support of this picture, we note that the extended tails of the non-Gaussian distributions become more prominent as the AR of the virus increases (Figure 11), which we expect exaggerates the difference in hydrodynamics between parallel and perpendicular modes. These differences in coupling are also likely to affect the dependence of the ensemble-averaged diffusivities on polymer concentration.

Scaling of the long-time diffusivity

To determine the effects of the multiple diffusive modes on the transport of viral nanoparticles, we compare the long-time translational diffusivities of the viruses (extracted from the ensemble-averaged MSDs in Figure 9) to those of spherical nanoparticles. The normalized diffusivities of spherical particles, for which the PDDs are Gaussian, collapse onto a single curve as a function of c/c^* (Figure 12) indicating that the dynamics of spherical nanoparticles follow the SE prediction obtained using the bulk viscosity. In sharp contrast, the virus diffusivities do not collapse on this SE master curve. Instead, the virus diffusivities are up to $30\times$ greater than the SE prediction.

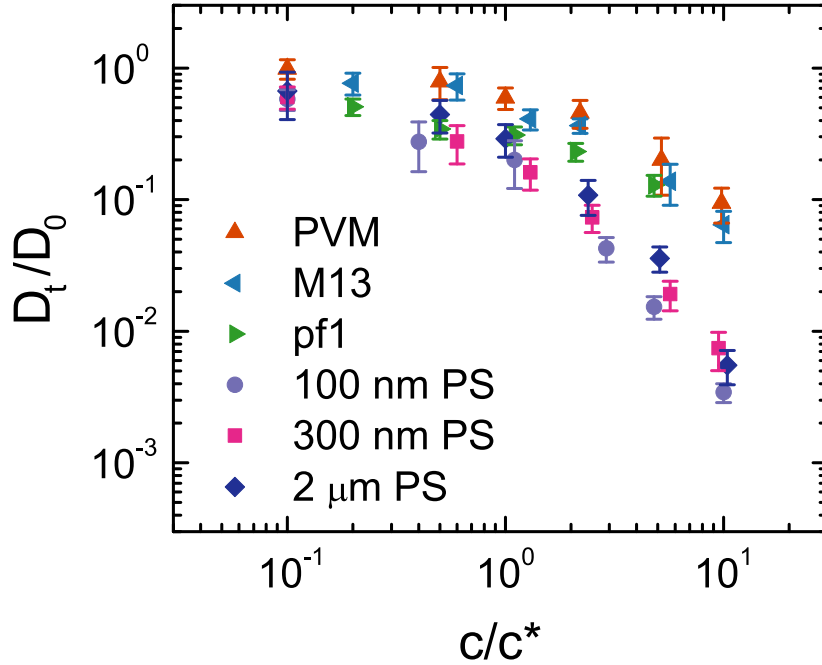


Figure 12: Normalized diffusivity D_t/D_0 as a function of normalized polymer concentration c/c^* for virus and spherical particles.

Faster-than-expected dynamics in polymer solutions have been observed for spherical nanoparticles whose size is comparable to length scales characterizing the polymer (R_g, ξ) [172, 197, 198]. In this size regime, the dynamics of the particles decouple from the solution viscosity and instead couple to the dynamics of the polymer chains

[105]. This coupling is controlled by the particle size, resulting in dynamics that collapse as a function of R/ξ . For anisotropic nanoparticles, however, it is not clear which length scale or scales control the particle diffusivity. The non-Gaussianity of the PDDs suggests that both the radius and length play a role in how filamentous viruses move through polymer solutions. We therefore examine the dependence of the diffusivity on R , L , and their combinations (Table 1).

Table 1: Different length scales S_i for PVM, M13, and pf1 virus particles.

| S_i [nm] | L | $2R$ | $\frac{L}{\ln(L/R)}$ | $\frac{R}{\ln(L/R)}$ | R_V | R_{SA} |
|------------|------|------|----------------------|----------------------|-------|----------|
| PVM | 200 | 13 | 58 | 3.8 | 29 | 25 |
| M13 | 900 | 6 | 160 | 1.0 | 29 | 37 |
| pf1 | 2000 | 6 | 310 | 0.9 | 38 | 55 |

We first examine the dependence of the normalized translational diffusivity D_t/D_0 on L/ξ and R/ξ (Figure 13(a),(b)). Neither ratio is able to collapse the virus diffusivities onto a single curve. Whereas L/ξ shifts the diffusivities of the high-AR (pf1) virus to larger length scales relative to those of the short-AR PVM, R/ξ conversely shifts PVM to larger effective length scales. We conclude that the controlling length scale must be intermediate between R and L .

In Newtonian liquids, the dynamics of rigid rods are dissimilar in directions parallel and perpendicular to the major axis due to differences in the hydrodynamic drag equations. The hydrodynamic modes average to produce a length scale of $L/\ln(L/R)$ [170] that controls the frictional drag and hence the translational diffusivity. Neither this length scale nor its radial counterpart $R/\ln(L/R)$, however, are able to collapse the diffusivity data for the viral nanoparticles onto a single curve (Figure 13(c),(d)). This result indicates that the ratio of the hydrodynamic drag forces acting in the directions parallel and perpendicular to the virus major axis is different in polymer

solutions than in Newtonian simple fluids. Further, it also indicates that the hydrodynamic radius of filamentous viruses, measured in 1x PBS (a Newtonian fluid), cannot be used to predict virus dynamics in semidilute polymer solutions.

Finally, a standard approach to determine the hydrodynamic forces on an anisotropic particle is to evaluate the frictional coefficients using a spherical particle of equivalent size as the basis for the Reynolds number Re_{eq} [202–205]. Inspired by this approach, we attempt to map the anisotropy of the viral nanoparticles onto spheres of equivalent size through two effective length scales $R_V = (3R^2L/4)^{1/3}$ and $R_{SA} = (RL/2)^{1/2}$ (Table 1). These length scales represent a sphere of equivalent volume or surface area to the virus, respectively. Both length scales collapse the normalized virus diffusivities onto a single curve within experimental error (Figure 13(e),(f)). Given the error in our measurements, we cannot conclude which of these length scales controls virus diffusion in semidilute polymer solutions. Nonetheless, both collapses support the idea that virus diffusivity depends on a weighted average of the radius and the length of the viral nanoparticle. This finding is consistent with the observation of non-Gaussian PDDs (Figure 10) and with the hypothesis that virus anisotropy leads to differences in the hydrodynamic drag forces that act on motions parallel and perpendicular to the long axis.

Conclusions

We measured the dynamics of three filamentous viruses in semidilute solutions of polymer using optical microscopy. Although the dynamics of the viral nanoparticles are diffusive on accessible time scales, the distributions of particle displacements are strikingly non-Gaussian and feature extended tails that become more pronounced as either polymer concentration or virus aspect ratio are increased. We attribute the non-Gaussian displacement distributions to the presence of multiple diffusive modes as filamentous viruses move along and normal to their major axis. These diffusive modes

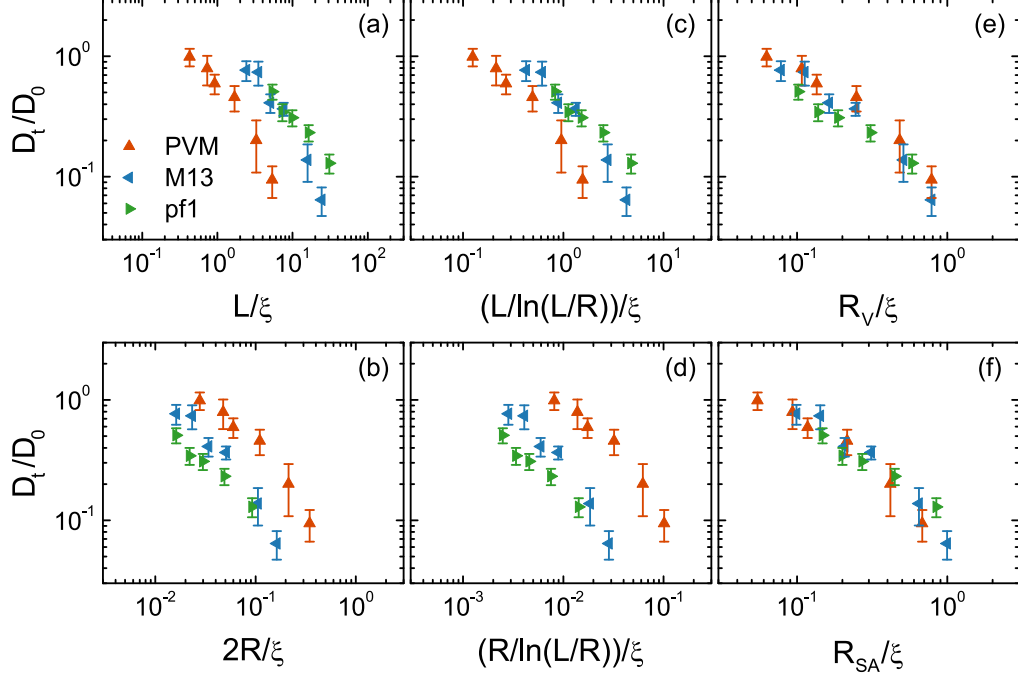


Figure 13: D_t/D_0 of the different virus species as a function of normalized length scale S_i/ξ where S_i are different virus length scales (Table 1) and where ξ is the polymer correlation length.

are different than those predicted by spherical or rigid rod scaling theories. Through these multiple diffusive modes, filamentous viruses are able to diffuse through semidilute polymer solutions over an order of magnitude faster than spherical nanoparticles of comparable size. The faster-than-expected diffusivities can be collapsed onto single curves according to effective length scales that are intermediate between R and L , consistent with the idea that filamentous viruses move through parallel and perpendicular motions.

Viruses are useful as tunable model systems for anisotropic particle transport in complex media, as their persistence length [206, 207] and contour length [208] can be modified by controlled mutation. Importantly, the filamentous viruses examined here, like λ -phage [209, 210], are semiflexible. Earlier studies on semiflexible carbon nanotubes showed that flexibility controlled their diffusion through polymer gels [200]. We speculate the differences in the diffusive modes of filamentous viruses are

related to the flexibility of the viral nanoparticles and the corresponding segmental dynamics[200, 201, 209, 210], and plan to explore the role of flexibility in future work.

CHAPTER 3: Isocratic Reporter-Exclusion Immunoassay Using Restricted-Access Adsorbents

Chromatographic analysis of drugs and biomolecules has become increasingly common in the last three decades [211–214]. When combined with mass spectrometry, column chromatographic techniques serve as powerful analytical platforms with excellent resolution, sensitivity, and reproducibility. Complex clinical and bioprocess samples usually require very high selectivity and substantial sample preparation before chromatographic analysis [215], however, posing obstacles to the broader use of standard modes of column chromatography. An alternative approach to detecting analytes in complex samples is an immunoassay, which uses antibodies and highly detectable reporters to achieve selectivity and sensitivity. One particularly robust form of immunoassay is the immuno-chromatographic lateral flow assay, best known as the basis of the home pregnancy test. In our previous work, we improved the sensitivity of an immuno-chromatographic lateral flow assay for MS2 virus detection using functionalized viral nanoparticles as reporters [147]. This approach gave superior limits of detection but is not suitable for routine, automated, and quantitative analyses in a central clinical laboratory or process analytical technology setting.

To address these issues, we explored the application of viral particles used in the lateral-flow format to a chromatographic assay format. The application of chromatographic methods in immunoassays has been extensively investigated over the last few decades. The most common technique, flow-injection analysis (FIA), has been used for immunoassay of many analytes [216]. FIA immunoassays usually are operated in either bind-elute or competitive displacement mode and require costly and often single-use affinity adsorbents [216–218]. Several researchers have addressed the challenges of developing wash-free immuno- and ligand-binding assays [219–222]. In previous work, we demonstrated a wash-free immunoassay based on the relocation

of chemiluminescent reporters above a light-blocking dye by flotation on antibody-modified microbubbles [223]. Using this concept, we developed a wash-free chromatographic immunoassay based on an analyte-dependent exclusion of reporter reagents from the restricted-access adsorbent CaptoTM Core 700. (Figure 14)

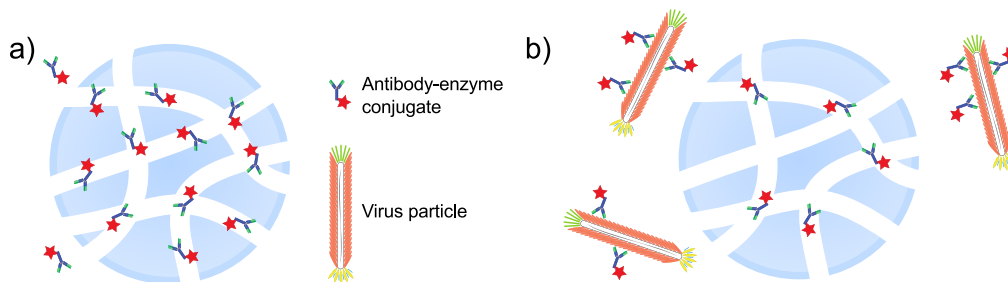


Figure 14: Schematic of reporter-exclusion assay for viruses. (a) In the absence of virus, smaller reporters can enter the core of the resin particles and bind to binding ligands. (b) In the presence of virus, reporters bind to analyte, are excluded from resin, and are detect in effluent.

Capto Core is a restricted-access adsorbent composed of two layers: a highly cross-linked agarose core with multimodal capture ligands and a porous outer shell with a size-exclusion cut off of 700 kDa (Figure 1a). The Capto multimodal octylamine ligand is sufficiently nonspecific to capture the great majority of interfering molecules and reporters with varying charge and hydrophobicity [224, 225]. At the same time, the size-restricted pores prevent larger objects from being captured. The combination of the size-exclusion and capture ligands has been mainly studied for the purification of viruses or virus-like particles [226–233]. The use of multimodal ligands in chromatography is usually accompanied by extensive pH and ionic strength screening [234–236], and mobile phase modifiers [237, 238]. In this study, we report the development of an isocratic immunodetection platform using Capto Core media to capture small reporters not bound to large or artificially-expanded analytes. Large analytes such as viruses can be detected directly by their ability to sequester small antibody-HRP conjugate reporters from capture in the adsorbent. Similarly, smaller analytes such as proteins can be detected by their ability to bridge reporter immunoconjugates

onto carrier particles large enough to be excluded from the adsorbent.

Materials and Methods

Cultivation of M13 phage

M13 phage was produced and titered as reported elsewhere.[147] Briefly, *E. coli* strain TG1 was grown to mid-log phase in Lysogeny broth (LB) medium. This pre-culture was then infected with M13 phage at 10^{12} M13 phage mL^{-1} , incubated at 37 °C for 2 hrs, then transferred to yeast extract tryptone (2xYT) medium and cultured overnight at 37 °C. After centrifugation, the sample was filtered through a 0.45 μm filter (Cat. No. 430512, Corning®) and subjected to polyethylene glycol (PEG)/salt precipitation with 20% w/v MW 3350 g mol^{-1} PEG in 2.5 M NaCl.

Reporter-exclusion assay for M13 phage using restricted-access adsorbent

All experiments were carried out at 4 °C on an AKTA purifier 10 using Capto Core 700 (Cat. No. 17548101, Cytiva, Uppsala, Sweden) resin packed in a glass HR 5/5 column (36 mm bed height; 5 mm inner diameter; 0.7 mL column volume) and equilibrated with 1x phosphate-buffered saline (PBS) at a linear flow velocity of 122 cm hr^{-1} . The bacteriophage M13 test analyte was incubated with (HRP)/Anti-M13 Monoclonal Conjugate (Cat. No. 27-9421-01, Cytiva, Uppsala, Sweden) at a final reagent concentration of 2.5 $\mu\text{g mL}^{-1}$. This mixture was supplemented with 2.5 μL of culture supernatant of nuclease-producing *Serratia marcescens* per mL of sample volume to eliminate possible assay interference due to free phage nucleic acids [158, 239]. After 1 hr of incubation, the 500 μL sample was loaded onto the column, which was washed with 15 column volumes (CVs) of PBS buffer. 1-mL fractions were collected and analyzed for HRP activity using 1-Step™ Ultra TMB-ELISA substrate (Cat. No. 34028, Thermo Fisher™ Scientific).

Immunochromatographic protein assay using restricted-access adsorbent

To extend the method to smaller protein analytes as well as larger viruses, human chorionic gonadotropin (hCG) was chosen as a model analyte. Goat anti- α -hCG polyclonal antibody (pAb) was conjugated to M13 phage as described previously [147]. Briefly, 100 μ L (10^{11}) M13 phage was suspended in 800 μ L 3 mM EDTA in PBS. 2-iminothiolane (Traut's reagent, Cat. No. 26101, Thermo Fisher Scientific) was added to a final concentration of 7 μ M, and the reaction was incubated for 90 min at 25 °C. Traut's reagent reacts with the primary amines of M13 phage coat proteins to introduce reactive sulfhydryl groups. Excess Traut's reagent was removed using ZebaTM Spin Desalting Columns, 7K MWCO (Cat. No. 89882, Thermo Fisher Scientific). Maleimide activation of the goat anti- α -hCG pAb was performed by mixing the antibody and sulfosuccinimidyl-4-(N-maleimidomethyl) cyclohexane-1-carboxylate (Sulfo-SMCC, Cat. No. 22322, Thermo Fisher Scientific) for 30 min at final concentrations of 22 μ M and 1.14 mM, respectively, in 1 mL PBS. Sulfo-SMCC is a water-soluble heterobifunctional amine-to-sulfhydryl cross-linking reagent with a sulfo-NHS ester group and a maleimide reactive group linked by a cyclohexane spacer. Excess sulfo-SMCC was removed using Zeba Spin Desalting Columns, 7K MWCO. Traut's reagent-modified M13 phage and sulfo-SMCC-modified pAb were then mixed for 90 min at 25 °C to allow coupling of the phage sulfhydryl groups to maleimide reactive groups on pAbs. Finally, uncoupled pAbs were removed using a 300 kDa Spectra/PorTM Float-A-Lyzer[®] (Cat. No. G235036, RepligenTM Corporation). The M13 anti-hCG conjugate (10^8 mL⁻¹) was incubated with 10 ng mL⁻¹ hCG in PBS for 30 min, followed by the addition of HRP/Anti- β hCG mAb conjugate (Thermo Fisher Scientific) to a final concentration of 2.8 μ g mL⁻¹. This mixture was supplemented with 5 Units mL⁻¹ of Benzonase Nuclease (Cat. No. 70746, Millipore SigmaTM). Commercial nuclease was chosen over the previous in-house nuclease to simplify sample prep and improve purity. The final mixture was incubated for 30 min at 25 °C. After

incubation, 500 μL of the mixture was loaded onto the Capto Core 700 column. The column had been pre-equilibrated with PBS, and the assay was performed with PBS at a linear flow velocity of 31 cm hr^{-1} (residence time 7 min). 1-mL fractions were collected and analyzed for HRP activity using 1-StepTM Ultra TMB-ELISA substrate (Cat. No. 34028, Thermo Fisher Scientific) and an ELISA plate reader (Tecan).

Results and Discussion

Reporter capture by restricted-access adsorbent

To evaluate the feasibility of developing a reporter-exclusion virus immunodetection platform, we first tested the efficiency of capturing free HRP/Anti-M13 conjugate by the adsorbent. In the absence of M13 phage, a control sample containing HRP/Anti-M13 conjugate was largely trapped in the ligand active core of the Capto Core resin, although a residual HRP background signal at 450 nm (Figure 15a, gray bars) and A280 (Figure 15a, blue trace) in early fractions suggested incomplete capture of HRP/Anti-M13 conjugate and possibly other proteins from the nuclease preparation. In the presence of M13 phage analyte (Figure 15b, gray bars), HRP/Anti-M13 conjugate bound to the phage was excluded from the adsorbent and detected in the eluted fractions. In volume fractions 4-6 (5-9 CVs), the HRP activity with analyte was at least $7\times$ that of the control without analyte.

To improve the completeness of reporter capture, these experiments were repeated at lower linear flow velocity (Figure 15c), 31 cm hr^{-1} , for a residence time of 7 min versus the previous 1.8 min, with the same bed height. At this linear flow velocity, 99% of the HRP/Anti-M13 conjugate HRP activity was captured compared to HRP/Anti-M13 control sample (Figure 15c, gray bars). This improvement shows that the Capto Core resin can capture nearly all the HRP/Anti-M13 conjugate, reducing the nonspecific signal from free reporter molecules.

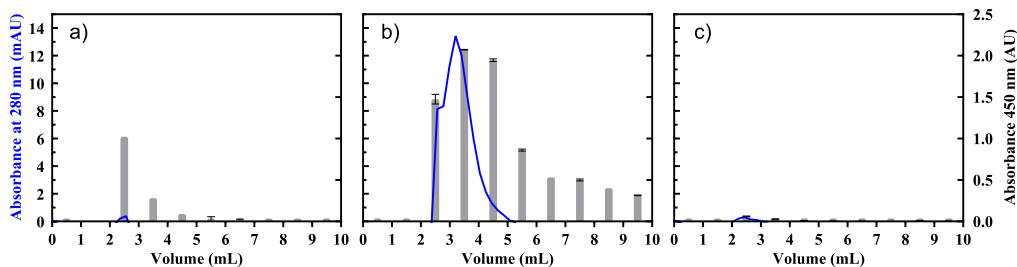


Figure 15: Absorbance at 280 nm (blue trace) and 450 nm (gray bar) of Capto Core column effluent as a function of volume fraction. (a) HRP/Anti-M13 at linear flow velocity 122 cm hr^{-1} ; (b) HRP/Anti-M13 and M13 at same linear flow velocity; (c) HRP/Anti-M13 at linear flow velocity 31 cm hr^{-1} .

Isocratic detection of M13 phage using restricted access adsorbent

Next, we tested the limit of detection of M13 phage particles with this assay. The reporter-exclusion assay was performed with 10^7 , 10^8 , and 10^9 M13 phage particles mL^{-1} in PBS with a linear flow velocity of 31 cm hr^{-1} (residence time 7 min). Figure 16 shows that the assay can detect 10^7 M13 phage particles mL^{-1} or less. In the absence of phage, the HRP/Anti-M13 conjugate was almost completely captured, resulting in low background HRP activity ($< 0.08 \text{ AU}$ measured at 450 nm). The highest HRP activity, obtained at a volume of 3 mL (4 CVs), was $5\times$, $18\times$ and $45\times$ that of the no-phage control for samples containing 10^7 , 10^8 , and 10^9 M13 phage particles mL^{-1} , respectively. The results demonstrate that, while free HRP/Anti-13 is nearly completely captured, the bound conjugate produces a strong signal in the presence of M13 phage.

Isocratic reporter-exclusion immunodetection of small protein analytes

The final size of the analyte-reporter complex is a critical aspect of a reporter-exclusion immunoassay using a restricted-access adsorbent. To enable the analysis of smaller analytes, we increased the size of the reporter-analyte complex by conjugating the capture antibody to the M13 phage. The functionalized M13 acts as a passive size-increasing carrier particle (Figure 17). Using a sandwich immunoassay format,

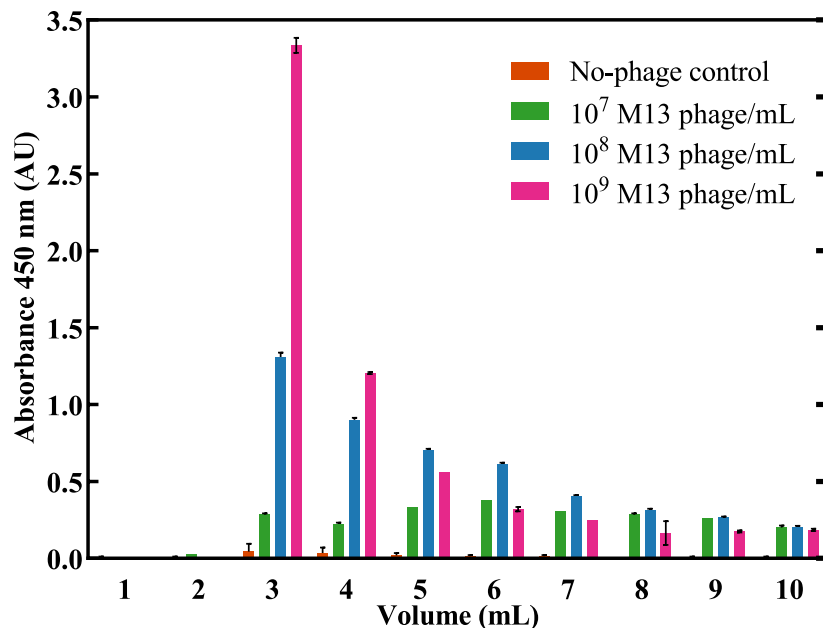


Figure 16: Absorbance at 450 nm of column effluent as a function of volume fraction with varying M13 concentrations at linear flow velocity 31 cm hr^{-1} .

the analyte is bound onto the large non-capturable phage particle, which then binds the small antibody-reporter conjugate. This complex is then a non-capturable carrier-analyte-reporter complex and only exists when the analyte is present. The assay was performed in PBS at a linear flow velocity of 31 cm hr^{-1} with a column bed height of 3.6 cm. The M13 carrier was conjugated with anti- α -hCG. The assay was run with 10^8 mL^{-1} functionalized M13 phage and 4.34×10^{12} molecules of HRP/Anti- β -hCG reporter ($1.4 \mu\text{g}$) in a $500 \mu\text{L}$ load volume.

To confirm capture of the HRP/Anti- β -hCG reporter, we ran the assay with only reporter conjugate (Figure 18, orange). We observed very low HRP activity similar to the results with the HRP/Anti-M13 assay confirming the capture of HRP/Anti- β -hCG conjugates. We then performed the assay with the functionalized M13 and the HRP/Anti- β -hCG. In the absence of hCG, we measured a low background signal (0.040 AU at 450 nm) as more than 99% of the HRP/Anti- β -hCG reporter was captured by the active core of the adsorbent (Figure 18, green). This is consistent with our previous results and confirms low nonspecific binding between the reporter

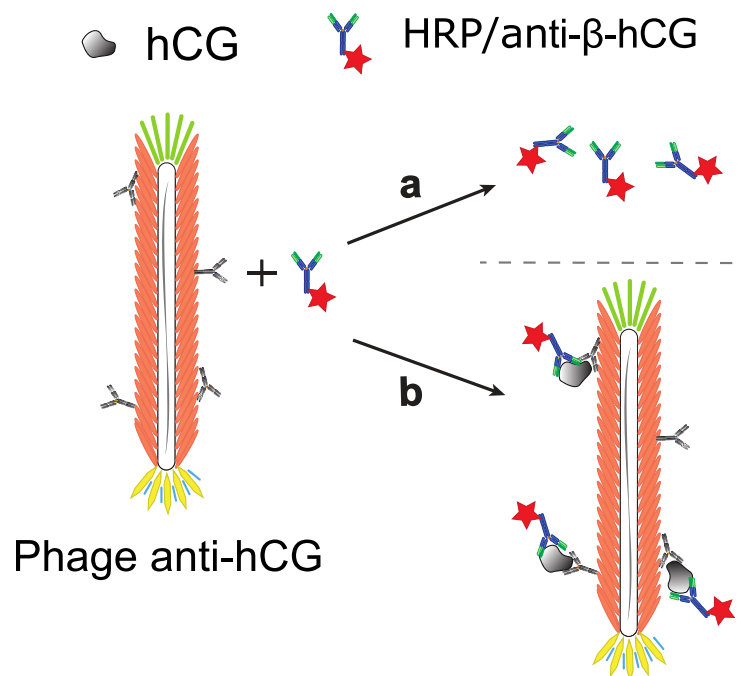


Figure 17: Schematic of the small-analyte reporter-exclusion immunoassay using restricted-access adsorbent. (a) In the absence of analyte, free reporter is captured by the adsorbent. (b) With analyte, analyte bridges the reporter to M13, and complex is excluded from adsorbent.

conjugate and the functionalized phage. In the presence of 10 ng mL^{-1} of hCG, the signal in fraction 2 (3 CVs) was at least $2.5\times$ higher than the negative control without hCG. This ratio was higher, up to $100\times$, in volume fractions 7 and 8. The results demonstrate the formation of the carrier-analyte-reporter complex and its exclusion from Capto Core resin.

We hypothesized that this platform could provide fast quantitation of viral titer at various stages of the vaccine manufacturing process. Specifically, it can be used to quantify the total virus content alongside the traditional TCID₅₀ (Tissue Culture Infectious Dose) assay to obtain a ratio of infectious to non-infectious viruses, e.g., in attenuated vaccines. The advantages of isocratic operation may also make the valuable platform in veterinary, agricultural, food, and environmental applications. A theoretical limitation of our approach is the saturation of the binding capacity of the Capto Core 700 adsorbent by high-protein samples such as blood or serum. Still,

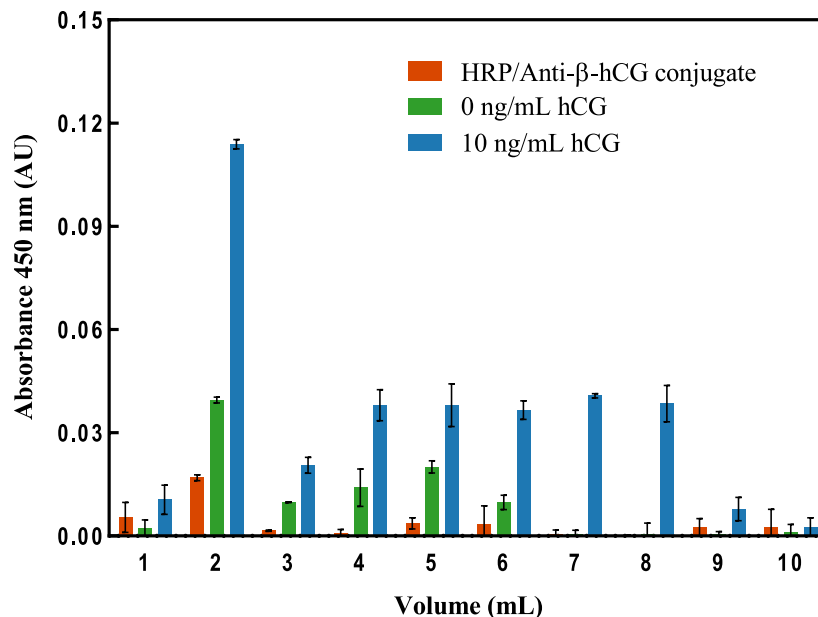


Figure 18: Absorbance at 450 nm of column effluent as a function of volume fraction at linear flow velocity 31 cm hr^{-1} for reporter conjugate only, reporter and Anti-hCG-M13, and reporter and Anti-hCG-M13 with 10 ng mL^{-1} hCG.

in practice, this is not expected to pose practical barriers. The samples of primary interest are urine, cell culture fluid, and serum with total protein concentrations of $6.2 \text{ mg } 100 \text{ mL}^{-1}$ [240], 2.8 mg mL^{-1} [241], and $60\text{-}80 \text{ mg mL}^{-1}$ [242], respectively. For the small column used here ($700 \mu\text{L}$), the dynamic binding capacity is $0.7 \text{ mL} \times 14.3 \text{ mg mL}^{-1}$ (10 mg) [243]. This implies that 160 mL , 3.6 mL , and $120\text{-}170 \mu\text{L}$ of urine, cell culture fluid, and serum, respectively, can be loaded on this relatively small and inexpensive column. A larger column could easily be used for increased binding capacity. Adsorbents with greater selectivity, such as antibody affinity matrices, also could overcome this difficulty, extending the advantages of this assay format to a wider variety of applications though at a higher cost.

Conclusions

In this work, we introduce an assay format utilizing restricted-access adsorbents as a generic assay format for the detection of viruses and small proteins. The assay transduces the presence of analyte into reporters being spared from capture by the

adsorbent. We use large virus particles as a mobile phase carrier to increase the size of the analyte-reporter complex and prevent capture by the adsorbent. We then measure the signal produced by the reporter in the column effluent to detect our analyte without extensive pH and ionic strength screening or mobile phase modifiers.

The readout time required for the colorimetric assay can be avoided by changing the enzymatic colorimetric reporters to either fluorescence or luminescence reporters, which might also allow simultaneous detection of distinct analytes by selecting reporter materials with different emission wavelengths. The M13 phage could be replaced in small-analyte assays with any other suitable nanoparticle small enough to traverse the column and large enough to be excluded from the capture resin. In the present work, we have utilized a pump-driven liquid chromatography system for flexibility during the initial assay demonstration. Still, more portable assays driven by gravity or a manual syringe could be developed along similar lines. In addition to supporting isocratic immunoassays, this approach can be generalized to a broad range of ligand-binding assays, using many types of reporters and recognition agents. The range of compatible modifications for this assay format demonstrates the potential of this format for a wide variety of applications.

CHAPTER 4: Conclusions and Future Directions

Conclusions and Future Directions for Virus Dynamics

Nanotechnology has become ubiquitous in many aspects of daily life and industrial processes. In particular, the healthcare sector continues to find new and innovative applications for the unique capabilities afforded by nanotechnology. Targeted drug delivery [43–45, 244], antifouling coatings [40–42], and enhanced imaging and biomolecular detection [46, 47, 49] are improving patient outcomes. Much of nanotechnology-based healthcare utilizes nanoparticles [44, 60, 75, 245], and this is especially the case for medical diagnostics. Nanoparticles can provide additional benefits due to the unique properties emergent at the nanoscale. Nanoscale enhanced properties, such as optical absorbance and high specific surface areas, improve the performance of nanoparticle-based systems and can increase the sensitivity of diagnostic techniques [80, 89, 246]. Beyond the inherent nanoscale properties, the transport of nanoparticles in often crowded and complex media plays a vital role in the performance of the diagnostic method [86, 247]. Therefore, understanding transport properties is critical to predicting performance and designing and improving medical diagnostics.

The transport properties of spherical nanoparticles in a crowded medium have been well studied [95–97]. Different models and theories are used to predict the effect of crowding on nanoparticle transport depending on the features of the specific system [98–106]. Not all nanoparticles of interest are spherical, and anisotropic shapes can alter the properties of the nanoparticles and be advantageous [107, 108, 110–113].

Many virus particles are anisotropic and have been incorporated into many different nanotechnology applications [121, 122, 132, 134]. Previous studies have shown the efficiency of viral nanoparticles in medical diagnostic assays as reporter particles in buffer solutions [147–149]. Real patient samples are often complex mixtures, and the effect of anisotropy on nanoparticle dynamics in these crowded solutions is not well understood.

We investigated the dynamics of three filamentous viral nanoparticles in a model polymer solution using fluorescence microscopy and particle tracking algorithms. We compared the dynamics of viral particles to spherical particles to observe the effect of anisotropy. We further examined the translation diffusivity of the viral particles using current theories of nanoparticle dynamics to explore the critical viral particle length scales controlling filamentous virus diffusion. We successfully dyed viral particles with fluorescent labels and imaged their quiescent diffusion. We then analyzed the resulting microscope videos with particle tracking algorithms to obtain the mean squared displacements (MSDs) and probability distribution of displacements (PDDs) of spherical fluorescent nanoparticles and the viral nanoparticles. Virus dynamics for all virus particles tested exhibited linear MSDs and non-Gaussian PDDs. This behavior is not observed with any spherical particles tested, which showed linear MSDs and Gaussian PDDs. The combination of linear MSDs and non-Gaussian PDDs has been seen in other crowded systems and is attributed to multiple modes of motion [105, 106, 185, 194–196]. Since this behavior is observed with the virus particle systems and not the spherical particle systems, we concluded that the anisotropic shape of the viruses is leading to these multiple modes of motion. Furthermore, we

extracted the translational diffusivity of the virus particles from the linear MSDs. Theories predicting nanoparticle diffusivity correlate the dynamics of nanoparticles with the dynamics of the surrounding environment, both of which scale with the ratio of their characteristic length scales [105]. With this framework, we examined the ratio of different possible virus length scales over polymer correlation lengths to determine the controlling virus length scale. We determined that the diffusivity data collapses with virus length scale that is a combination of virus length L and radius R . This result reinforces our hypothesis that the virus anisotropy controls virus dynamics in these crowded systems.

Understanding viral nanoparticle dynamics is critical for designing new applications for virus particles in nanotechnology. We studied the dynamics of the filamentous virus particles and have shown that the anisotropy of these particles gives rise to multiple modes of motion. The anisotropic shape also controls the translational diffusivity of these particles in a crowded medium. These results help us understand how shape impacts diffusion of filamentous nanoparticles and open new directions for further research.

While the combination of linear MSDs and non-Gaussian PDDs indicate multiple modes of motion for virus diffusion, the limitations of the microscope setup prevent the complete characterization of these modes of motion. As observed in other systems involving filaments, the effects of chain ends can dominate filament dynamics through reptation [201, 248–250]. This effect may also be present for filamentous viral particles as well. Enhanced visualization of the virus particles can allow the characterization of the virus modes of motion by resolving the shape of the virus during diffusion.

Previous studies on the dynamics of biopolymers imaged filaments with subpixel resolution through image processing techniques [251]. With more precise imaging of the virus particle, tracking the ends of the particles can offer improved analysis of the rotational diffusivity or reptation of the filament ends.

In these experiments, the dynamics of three virus particles of different sizes and aspect ratios were examined, but this represents only a small fraction of the total biodiversity of even the filamentous viruses. Many viruses, however, are prohibitively challenging to grow on an industrial scale due to the biological hazard posed by the virus or host cell [252–254]. This limits the possible range of viruses that can be studied for future applications. Viruses, however, can be altered through mutagenesis. Due to the nature of virus replication, changing a virus DNA/RNA will change the viral proteins that are synthesized and can alter the properties of the virus particle [141, 255–257]. Researchers have created mutant viral particles for various applications and have developed proven techniques for incorporating mutant genes [258, 259]. By utilizing mutagenesis techniques, viruses that are relatively simple to produce can exhibit the desired properties. Several mutants of group Ff viruses, which include M13, have already been studied [177, 208, 255, 260, 261]. Further exploration of possible M13 mutants can expand research into the effects of other filamentous virus properties, like filament persistence length, on virus diffusion through crowded solutions.

The insights gained by studying viral nanoparticle dynamics also need to be applied to the practical design of LFAs and LFA reporters. As discussed previously, reporter transport plays a critical role in the performance of the LFA [89, 262–264].

LFAs wick sample fluid by capillary action through the porous LFA membrane, and reporter particles bind to the surface of these pores. Furthermore, the binding of reporters from the bulk fluid to the functionalized pore surface is often modeled as a surface-mediated reaction with binding affinities based on the different components of the full LFA. While previous work has demonstrated the efficacy of viral nanoparticles as LFA reporters, the experiments were run with buffer solutions [147–149, 175]. Real medical samples are complex mixtures of cells, proteins, polysaccharides, and other components [265–269]. Many diagnostic assays utilize pre-assay sample preparation to reduce undesirable components or increase the analyte concentration [268–271]. Elaborate sample preparation techniques may only be feasible in centralized facilities with access to specialized equipment and trained personnel. Assays need to operate effectively with less sample preparation to transition more diagnostics out of central laboratories. This specification will result in LFAs needing to run with complex mixtures. LFA studies of filamentous virus reporter performance in either a model or real medical sample can be compared with the proposed virus diffusivity scaling. If reporter performance and diffusivity scaling are correlated, new virus particles can be selected as LFA reporters using the virus size and shape to predict their performance as reporters.

Conclusions and Future Directions for Size-Exclusion Assay

The possibilities of virus reporters extend beyond assays that rely on immobilizing the reporter particle. As discussed earlier, anisotropic particles have higher surface areas per particle, which can correlate with reporter performance in the LFA format

[147–149, 160]. Filamentous viruses are also very large compared to many analytes of interest. Therefore, virus particles can be used in size-based assays. Size-exclusion resins are commonly used in polymer synthesis and bioprocessing and are relatively inexpensive compared to affinity-based chromatography [272]. The principle of size-exclusion correlates the resin pore size and the residence times of individual components in a sample. Size-exclusion resins are made of fine porous beads and are packed into a column bed. This configuration generates two populations of pores through the column, the smaller pores in the beads and the larger interstitial pores from imperfect bead packing. When a polydisperse mixture flows through the column, components smaller than the bead pore flow through the smaller pores while larger components only flow through the larger pores. The more tortuous path through small pores increases the residence time in the column for smaller components. This process results in separation based on component size. The separation can be enhanced using capture ligands in the pores to isolate small components from the stream. The challenge of size-exclusion assays, however, is nonspecificity. Many proteins have similar sizes and similar spectral properties, making separation and detection of specific proteins difficult. We can change the range of pore sizes available to the protein by binding it to a larger object. A detection step can then generate a signal when the analyte of interest binds to the reporter.

We developed an isocratic immunoassay using CaptoTMCore 700, a size-exclusion adsorbent. The adsorbent comprises two layers, a size-exclusion porous outer shell with molecular weight cutoff MWCO = 700 kDa and an agarose core with multimodal (hydrophobic + anion-exchange) capture ligands. The column then operates by ex-

cluding larger components from the resin core while smaller components enter the core and are captured. As a proof-of-concept, we selected bacteriophage (phage) M13 as a model analyte and detect M13 with an antibody reporter molecule, peroxidase (HRP)/anti-M13. We successfully detected M13 in column effluent at concentration of 10^7 phage mL^{-1} over a range of column volume fractions with almost all reporter molecules captured by the column in the absence of M13. This assay demonstrates that the binding of reporter molecules to the phage particle prevents reporter capture by the resin core, generating a signal in the effluent. We also demonstrated the more general efficacy of this assay format by detecting a relatively small model protein, human chorionic gonadotropin (hCG). M13 particles functionalized with anti-hCG acted as a scaffold for binding hCG and HRP/anti-hCG. This complex prevented hCG or HRP/anti-hCG from entering and binding in the resin core. The assay demonstrated a strong signal ratio (positive over negative) with 10 ng mL^{-1} hCG. While early fractions produced a higher overall signal, the positive to negative ratio increased from $2.5\times$ in earlier volume fractions to over $100\times$ in later-eluting fractions.

Isocratic immunoassays have potential in many bioprocessing and diagnostics applications. We have shown that filamentous M13 is a viable mobile phase binding scaffold. Using size-restrictive adsorbents, we can detect a range of different analytes of interest in a semi-continuous process. Further development of this assay can demonstrate the optimal process parameters for practical applications.

For the proof-of-concept experiments, the analyte was added to buffer solutions. Real samples of interest, however, will be complex solutions. For diagnostic applications, a sufficient quantity of blood or urine can be readily collected to perform

assays in this proposed format. For bioprocessing, analysis of cell culture solutions is critical to ensure product purity. Protein levels of these samples can vary between 0.06 and 60 mg mL⁻¹ with variable salt concentration and pH levels [240–242]. Understanding the impact of different sample compositions is necessary for any future application of this technology. Optimal process parameters, like flow rate, sample dilution, additives, etc., and process tolerances can change between sample types and target analytes. A design of experiments approach will improve screening of critical assay parameters and support implementation of this assay format to a broader range of applications.

Along with optimizing the assay parameters, studying the detection of different analytes of interest is also essential to demonstrate the efficacy of this assay. While we have shown detection of the model protein hCG, many other analytes are also critical to applying this assay for different applications. In the context of healthcare, different protein biomarkers or virus particles correspond to different diseases. For diagnostic applications, a generic assay format needs to work with a range of analytes. These biomarkers and viruses can be present in various biological samples at different concentrations. Exploratory experiments using various model proteins and virus particles of varying sizes with the corresponding sample can demonstrate the suitability of this assay format for other diagnostic targets.

Furthermore, bioprocessing often needs to purify valuable biomolecules from among a large mixture of proteins, cell lysate, and other macromolecules. Product loss through imperfect separation and recovery represents a significant loss of revenue [273–276]. Identifying product proteins in a mixture of different proteins is crit-

ical to addressing this problem. Most protein characterization techniques require some sidestream collection and analysis. [275, 276] This assay can be easily incorporated into existing purification processes to detect product breakthroughs on-site. To demonstrate this, a purification process, like an affinity column, can run with a model protein mixture and then be studied with this size-exclusion assay. These results can then be compared to more traditional protein analytical methods for accuracy and efficiency.

While this study examined a single-analyte sample, size-exclusion assays can be extended to multiplex detection. Virus particles can be functionalized with different binding motifs. A mixture of viruses modified with different binding motifs can then exclude several analytes from the mixture simultaneously. The assay can then be configured for different signaling methods, like enzymes with specific substrates or fluorescence molecules with different emission wavelengths, such as quantum dots. The results from the assay can be integrated into different signal combinations based on the assay requirements. Results can include all analytes, one analyte but not others, or some collection of analytes. The possibility of multiplexing provides an opportunity to adapt this assay format to many applications while still maintaining a relatively lower cost.

Bibliography

- (1) Kost, G. J. *American Journal of Clinical Pathology* **1995**, *104*, S111–S127.
- (2) Tsui, P. T.; Kwok, M. L.; Yuen, H.; Lai, S. T. *Emerging Infectious Diseases* **2003**, *9*, 1064–1069.
- (3) Epner, P. L.; Gans, J. E.; Graber, M. L. *BMJ Quality and Safety* **2013**, *22*, ii6–ii10.
- (4) Land, K. J.; Boeras, D. I.; Chen, X.-S.; Ramsay, A. R.; Peeling, R. W. *Nature Microbiology* **2019**, *4*, 46–54.
- (5) Mardani, R.; Vasmehjani, A. A.; Zali, F.; Gholami, A.; Mousavi Nasab, S. D.; Kaghazian, H.; Kaviani, M.; Ahmadi, N. *Archives of Academic Emergency Medicine* **2020**, *8*, e43.
- (6) Feynman, R. P. *Engineering and Science* **1960**, *23*, 22–26, 30, 34, 36.
- (7) NNI National Nanotechnology Initiative.
- (8) Roduner, E. *Chemical Society Reviews* **2006**, *35*, 583–592.
- (9) Otto, D. P.; De Villiers, M. M. *Nanotechnology Reviews* **2013**, *2*, 171–199.
- (10) Dolez, P. I. In *Nanoengineering - Global Approaches to Health and Safety Issues*, 2015, pp 3–40.
- (11) Zambon, A.; Córdoba, M. *Foundations of Science* **2021**, DOI: 10 . 1007 / s10699-020-09723-8.

- (12) Roco, M. C. *Journal of Nanoparticle Research* **2001**, *3*, 353–360.
- (13) Chen, H.; Roco, M. C.; Li, X.; Lin, Y. *Nature Nanotechnology* **2008**, *3*, 123–125.
- (14) Coccia, M.; Finardi, U.; Margon, D. *Journal of Technology Transfer* **2012**, *37*, 777–787.
- (15) Singh, N. A. *Environmental Chemistry Letters* **2017**, *15*, 185–191.
- (16) Zhu, W.; Bartos, P. J.; Porro, A. *Materials and Structures/Materiaux et Constructions* **2004**, *37*, 649–658.
- (17) Sanchez, F.; Sobolev, K. *Construction and Building Materials* **2010**, *24*, 2060–2071.
- (18) Weiss, J.; Takhistov, P.; McClements, D. J. *Journal of Food Science* **2006**, *71*, 107–116.
- (19) Derosa, M. C.; Monreal, C.; Schnitzer, M.; Walsh, R.; Sultan, Y. *Nature Nanotechnology* **2010**, *5*, 91.
- (20) Sekhon, B. S. *Nanotechnology, Science and Applications* **2010**, *3*, 1–15.
- (21) He, X.; Deng, H.; min Hwang, H. *Journal of Food and Drug Analysis* **2019**, *27*, 1–21.
- (22) Serrano, E.; Rus, G.; García-Martínez, J. *Renewable and Sustainable Energy Reviews* **2009**, *13*, 2373–2384.
- (23) Wang, Z. L.; Wu, W. *Angewandte Chemie - International Edition* **2012**, *51*, 11700–11721.

- (24) Abdalla, A. M.; Elnaghi, B. E.; Hossain, S.; Dawood, D.; Abdelrehim, O.; Azad, A. K. *Advanced Energy Conversion Materials* **2020**, *1*, 30–54.
- (25) Bryant, S. T.; Straker, K.; Wrigley, C. *Journal of Cleaner Production* **2020**, *244*, 118725.
- (26) Bera, A.; Belhaj, H. *Journal of Natural Gas Science and Engineering* **2016**, *34*, 1284–1309.
- (27) Cheraghian, G.; Hendraningrat, L. *International Nano Letters* **2016**, *6*, 1–10.
- (28) Peng, B.; Tang, J.; Luo, J.; Wang, P.; Ding, B.; Tam, K. C. *Canadian Journal of Chemical Engineering* **2018**, *96*, 91–100.
- (29) Hemmingson, S. L.; Campbell, C. T. *ACS Nano* **2017**, *11*, 1196–1203.
- (30) *Nanotechnology in Catalysis: Applications in the Chemical Industry, Energy Development, and Environment Protection*; Sels, B. F., Van de Voorde, M., Eds.; John Wiley and Sons: Newark, 2017, p 1190.
- (31) Višić, B.; Panchakarla, L. S.; Tenne, R. *Journal of the American Chemical Society* **2017**, *139*, 12865–12878.
- (32) Berglund, L. A.; Burgert, I. *Advanced Materials* **2018**, *30*, 1704285.
- (33) Kumar, V. V.; Balaganesan, G.; Lee, J. K. Y.; Neisiany, R. E.; Surendran, S.; Ramakrishna, S. *Polymers* **2019**, *11*, 644.
- (34) Wang, Y.; Jiang, D.; Zhang, L.; Li, B.; Sun, C.; Yan, H.; Wu, Z.; Liu, H.; Zhang, J.; Fan, J.; Hou, H.; Ding, T.; Guo, Z. *Nanotechnology* **2020**, *31*, 025704.

- (35) Badi, N.; Lutz, J.-F. *Chemical Society Reviews* **2009**, *38*, 3383–3390.
- (36) Ayres, N. *Polymer Chemistry* **2010**, *1*, 769–777.
- (37) Cameron, D. J. A.; Shaver, M. P. *Chemical Society Reviews* **2011**, *10*, 1761–1776.
- (38) Maria de Souza Antunes, A.; Simone de Menezes Alencar, M.; Henrique da Silva, C.; Nunes, J.; Maria Lins Mendes, F. *Recent Patents on Nanotechnology* **2011**, *6*, 29–43.
- (39) Wallace, G. G.; Higgins, M. J.; Moulton, S. E.; Wang, C. *Nanoscale* **2012**, *4*, 4327–4347.
- (40) Polívková, M.; Hubáček, T.; Staszek, M.; Švorčík, V.; Siegel, J. *International Journal of Molecular Sciences* **2017**, *18*, DOI: 10.3390/ijms18020419.
- (41) Ramos, A. P.; Cruz, M. A.; Tovani, C. B.; Ciancaglini, P. *Biophysical Reviews* **2017**, *9*, 79–89.
- (42) Huang, W.; Ling, S.; Li, C.; Omenetto, F. G.; Kaplan, D. L. *Chemical Society Reviews* **2018**, *47*, 6486–6504.
- (43) Mazzola, L. *Nature Biotechnology* **2003**, *21*, 1137–1143.
- (44) De Jong, W. H.; Borm, P. J. A. *International Journal of Nanomedicine* **2008**, *3*, 133–149.
- (45) Farokhzad, O. C.; Langer, R. *ACS Nano* **2009**, *3*, 16–20.
- (46) Nie, S.; Xing, Y.; Kim, G. J.; Simons, J. W. *Annual Review of Biomedical Engineering* **2007**, *9*, 257–288.

- (47) Hartman, M. R.; Ruiz, R. C. H.; Hamada, S.; Xu, C.; Yancey, K. G.; Yu, Y.; Han, W.; Luo, D. *Nanoscale* **2013**, *5*, 10141.
- (48) Reinholt, S. J.; Sonnenfeldt, A.; Naik, A.; Frey, M. W.; Baeumner, A. J. *Analytical and Bioanalytical Chemistry* **2014**, *406*, 3297–3304.
- (49) Syedmoradi, L.; Daneshpour, M.; Alvandipour, M.; Gomez, F. A.; Hajghassem, H.; Omidfar, K. *Biosensors and Bioelectronics* **2017**, *87*, 373–387.
- (50) Inshakova, E.; Inshakov, O. *MATEC Web of Conferences* **2017**, *129*, 02013.
- (51) Inshakova, E.; Inshakova, A.; Goncharov, A. In *IOP Conference Series: Materials Science and Engineering*, IOP Publishing: 2020; Vol. 971, p 032031.
- (52) Pillai, R. G.; Bezbaruah, A. N. *Journal of Nanoparticle Research* **2017**, *19*, 41.
- (53) Tsang, M. P.; Kikuchi-uehara, E.; Sonnemann, G. W.; Aymonier, C.; Hirao, M. *Nature Nanotechnology* **2017**, *12*, 734–739.
- (54) Malik, R.; Patil, S. *Applied Clinical Research, Clinical Trials and Regulatory Affairs* **2020**, *7*, 225–236.
- (55) Pikula, K.; Zakharenko, A.; Chaika, V.; Kirichenko, K.; Tsatsakis, A.; Golokhvast, K. *Current Opinion in Toxicology* **2020**, *19*, 1–6.
- (56) Rajput, N. *International Journal of Engineering and Technology* **2015**, *7*, 1806–1811.
- (57) Kumar K, H.; Venkatesh, N.; Bhowmik, H.; Kuila, A. *Biomedical Journal of Scientific and Technical Research* **2018**, *4*, 3765–3775.

- (58) Stark, W. J.; Stoessel, P. R.; Wohlleben, W.; Hafner, A. *Chemical Society Reviews* **2015**, *44*, 5793–5805.
- (59) Beyene, H. D.; Werkneh, A. A.; Bezabh, H. K.; Ambaye, T. G. *Sustainable Materials and Technologies* **2017**, *13*, 18–23.
- (60) Kumar, R.; Lal, S. *Journal of Nanomaterials and Molecular Nanotechnology* **2014**, *3*, 10000150.
- (61) Dave, V.; Tak, K.; Sohgaure, A.; Gupta, A.; Sadhu, V.; Reddy, K. R. *Journal of Microbiological Methods* **2019**, *160*, 130–142.
- (62) Mishra, P. K.; Ekielski, A. *Nanomaterials* **2019**, *9*, 243.
- (63) Vijayaraghavan, K.; Ashokkumar, T. *Journal of Environmental Chemical Engineering* **2017**, *5*, 4866–4883.
- (64) Khan, A. U.; Malik, N.; Khan, M.; Cho, M. H.; Khan, M. M. *Bioprocess and Biosystems Engineering* **2018**, *41*, 1–20.
- (65) Krajina, B. A.; Proctor, A. C.; Schoen, A. P.; Spakowitz, A. J.; Heilshorn, S. C. *Progress in Materials Science* **2018**, *91*, 1–23.
- (66) Xu, S.; Zhong, G.; Chen, C.; Zhou, M.; Kline, D. J.; Jacob, R. J.; Xie, H.; He, S.; Huang, Z.; Dai, J.; Brozena, A. H.; Shahbazian-Yassar, R.; Zachariah, M. R.; Anlage, S. M.; Hu, L. *Matter* **2019**, *1*, 759–769.
- (67) Ealias, A. M.; Saravanakumar, M. P. *IOP Conference Series: Materials Science and Engineering* **2017**, *263*, 032019.
- (68) Moshfegh, A. Z. *Journal of Physics D: Applied Physics* **2009**, *42*, 233001.

- (69) Neyts, E. C.; Ostrikov, K.; Sunkara, M. K.; Bogaerts, A. *Chemical Reviews* **2015**, *115*, 13408–13446.
- (70) Deshmukh, S. P.; Patil, S. M.; Mullani, S. B.; Delekar, S. D. *Materials Science and Engineering C* **2019**, *97*, 954–965.
- (71) Crosby, A. J.; Lee, J. Y. *Polymer Reviews* **2007**, *47*, 217–229.
- (72) Suttiponparnit, K.; Jiang, J.; Sahu, M.; Suvachittanont, S.; Charinpanitkul, T.; Biswas, P. *Nanoscale Research Letters* **2011**, *6*, 27.
- (73) Guo, D.; Xie, G.; Luo, J. *Journal of Physics D: Applied Physics* **2014**, *47*, DOI: 10.1088/0022-3727/47/1/013001.
- (74) Cordeiro, M.; Carlos, F. F.; Pedrosa, P.; Lopez, A.; Baptista, P. V. *Diagnostics* **2016**, *6*, 1–20.
- (75) Sengani, M.; Grumezescu, A. M.; Rajeswari, V. D. *OpenNano* **2017**, *2*, 37–46.
- (76) Li, S.; Meng Lin, M.; Toprak, M. S.; Kim, D. K.; Muhammed, M. *Nano Reviews* **2010**, *1*, 5214.
- (77) Issa, B.; Obaidat, I. M.; Albiss, B. A.; Haik, Y. *International Journal of Molecular Sciences* **2013**, *14*, 21266–21305.
- (78) Welch, C. M.; Compton, R. G. *Analytical and Bioanalytical Chemistry* **2006**, *384*, 601–619.
- (79) Ghaderi, S.; Ramesh, B.; Seifalian, A. M. *Journal of Drug Targeting* **2011**, *19*, 475–486.
- (80) Petryayeva, E.; Algar, W. R. *RSC Advances* **2015**, *5*, 22256–22282.

- (81) Hanemann, T.; Szabó, D. V. *Materials* **2010**, *3*, 3468–3517.
- (82) Chakraborti, S.; Joshi, P.; Chakravarty, D.; Shanker, V.; Ansari, Z. A.; Singh, S. P.; Chakrabarti, P. *Langmuir* **2012**, *28*, 11142–11152.
- (83) Kim, S. T.; Saha, K.; Kim, C.; Rotello, V. M. *Accounts of Chemical Research* **2013**, *46*, 681–691.
- (84) Chaudhuri, R. G.; Paria, S. *Chemical Reviews* **2012**, *112*, 2373–2433.
- (85) Jazayeri, M. H.; Amani, H.; Pourfatollah, A. A.; Pazoki-Toroudi, H.; Sedighimoghaddam, B. *Sensing and Bio-Sensing Research* **2016**, *9*, 17–22.
- (86) Kairdolf, B. A.; Qian, X.; Nie, S. *Analytical Chemistry* **2017**, *89*, 1015–1031.
- (87) Gorky, F.; Best, A.; Jasinski, J.; Allen, B. J.; Alba-Rubio, A. C.; Carreon, M. L. *Journal of Catalysis* **2021**, *393*, 369–380.
- (88) Quesada-González, D.; Merkoçi, A. *Biosensors and Bioelectronics* **2015**, *73*, 47–63.
- (89) Zhan, L.; Guo, S.-Z.; Song, F.; Gong, Y.; Xu, F.; Boulware, D. R.; Mcalpine, M. C.; Chan, W. C. W.; Bischof, J. C. *Nano Letters* **2017**, *17*, 7207–7212.
- (90) Shah, S.; Liu, Y.; Hu, W.; Gao, J. *Journal of Nanoscience and Nanotechnology* **2011**, *11*, 919–928.
- (91) Cheraghian, G.; Hendraningrat, L. *International Nano Letters* **2016**, *6*, 129–138.
- (92) Casati, R.; Vedani, M. *Metals* **2014**, *4*, 65–83.

- (93) Bizmark, N.; Schneider, J.; Priestley, R. D.; Datta, S. S. *Science Advances* **2020**, *6*, 1–11.
- (94) Bird, R. B.; Stewart, W. E.; Lightfoot, E. N., *Transport Phenomena: Volume 1*, 2nd; John Wiley and Sons: Hoboken, NJ, 2006, p 928.
- (95) Mackay, M. E.; Dao, T. T.; Tuteja, A.; Ho, D. L.; Van Horn, B.; Kim, H. C.; Hawker, C. J. *Nature Materials* **2003**, *2*, 762–766.
- (96) Tuteja, A.; Mackay, M. E.; Narayanan, S.; Asokan, S.; Wong, M. S. *Nano Letters* **2007**, *7*, 1276–1281.
- (97) Pryamitsyn, V.; Ganesan, V. *Journal of Polymer Science, Part B: Polymer Physics* **2016**, *54*, 2145–2150.
- (98) Ogston, A. G. *Transactions of the Faraday Society* **1958**, *54*, 1754–1757.
- (99) Altenberger, A. R.; Tirrell, M. *The Journal of Chemical Physics* **1983**, *80*, 2208–2213.
- (100) Johansson, L.; Elvingson, C.; Löfroth, J. E. *Macromolecules* **1991**, *24*, 6024–6029.
- (101) Cukier, R. I. *Macromolecules* **1984**, *17*, 252–255.
- (102) Phillies, G. D.; Ullmann, G. S.; Ullmann, K.; Lin, T. H. *The Journal of Chemical Physics* **1985**, *82*, 5242–5246.
- (103) Cheng, Y.; Prud'homme, R. K.; Thomas, J. L. *Macromolecules* **2002**, *35*, 8111–8121.

- (104) Brochard Wyart, F.; de Gennes, P. *The European Physical Journal E - Soft Matter* **2000**, *1*, 93–97.
- (105) Cai, L. H.; Panyukov, S.; Rubinstein, M. *Macromolecules* **2011**, *44*, 7853–7863.
- (106) Cai, L. H.; Panyukov, S.; Rubinstein, M. *Macromolecules* **2015**, *48*, 847–862.
- (107) Sajjanlal, P. R.; Sreeprasad, T. S.; Samal, A. K.; Pradeep, T. *Nano Reviews* **2011**, *2*, 5883.
- (108) Li, N.; Zhao, P.; Astruc, D. *Angewandte Chemie - International Edition* **2014**, *53*, 1756–1789.
- (109) Lisjak, D.; Mertelj, A. *Progress in Materials Science* **2018**, *95*, 286–328.
- (110) Thorkelsson, K.; Bai, P.; Xu, T. *Nano Today* **2015**, *10*, 48–66.
- (111) Chau, M.; De France, K. J.; Kopera, B.; Machado, V. R.; Rosenfeldt, S.; Reyes, L.; Chan, K. J.; Förster, S.; Cranston, E. D.; Hoare, T.; Kumacheva, E. *Chemistry of Materials* **2016**, *28*, 3406–3415.
- (112) Patzke, G. R.; Krumeich, F.; Nesper, R. *Angewandte Chemie - International Edition* **2002**, *41*, 2446–2461.
- (113) Priecel, P.; Salami, H. A.; Padilla, R. H.; Zhong, Z.; Lopez-Sanchez, J. A. *Chinese Journal of Catalysis* **2016**, *37*, 1619–1650.
- (114) Stanley, W. M. *Science* **1935**, *81*, 644–645.
- (115) Von Borries, B.; Ruska, E.; Ruska, H. *Klinische Wochenschrift* **1938**, *17*, 921–925.

- (116) Lefkowitz, E. J.; Dempsey, D. M.; Hendrickson, R. C.; Orton, R. J.; Siddell, S. G.; Smith, D. B. *Nucleic Acids Research* **2018**, *46*, D708–D717.
- (117) Hatcher, E. L.; Zhdanov, S. A.; Bao, Y.; Blinkova, O.; Nawrocki, E. P.; Ostapchuck, Y.; Schaffer, A. A.; Rodney Brister, J. *Nucleic Acids Research* **2017**, *45*, D482–D490.
- (118) Breitbart, M.; Rohwer, F. *Trends in Microbiology* **2005**, *13*, 278–284.
- (119) Anthony, S. J.; Epstein, J. H.; Murray, K. A.; Navarrete-Macias, I.; Zambrana-Torrel, C. M.; Solovyov, A.; Ojeda-Flores, R.; Arrigo, N. C.; Islam, A.; Khan, S. A.; Hosseini, P.; Bogich, T. L.; Olival, K. J.; Sanchez-Leon, M. D.; Karesh, W. B.; Goldstein, T.; Luby, S. P.; Morse, S. S.; Mazet, J. A.; Daszak, P.; Lipkin, W. I. *mBio* **2013**, *4*, e00598–13.
- (120) Sepulveda, B. P.; Redgwell, T.; Rihtman, B.; Pitt, F.; Scanlan, D. J.; Millard, A. *FEMS Microbiology Letters* **2016**, *363*, fnw158.
- (121) Wen, A. M.; Steinmetz, N. F. *Chemical Society Reviews* **2016**, *45*, 4074–4126.
- (122) Singh, P.; Gonzalez, M. J.; Manchester, M. *Drug Development Research* **2006**, *67*, 23–41.
- (123) Hull, R. In *Plant Virology*, Minihane, C., Mullane, C., Eds., 5th ed.; Academic Press: Oxford, UK, 2014; Chapter 3, pp 69–143.
- (124) Lee, K. L.; Hubbard, L. C.; Hern, S.; Yildiz, I.; Gratzl, M.; Steinmetz, N. F. *Biomaterials Science* **2013**, *1*, 581–588.

- (125) Kendall, A.; McDonald, M.; Bian, W.; Bowles, T.; Baumgarten, S. C.; Shi, J.; Stewart, P. L.; Bullitt, E.; Gore, D.; Irving, T. C.; Havens, W. M.; Ghabrial, S. A.; Wall, J. S.; Stubbs, G. *Journal of Virology* **2008**, *82*, 9546–9554.
- (126) Clokie, M. R.; Millard, A. D.; Letarov, A. V.; Heaphy, S. *Bacteriophage* **2011**, *1*, 31–45.
- (127) Dogic, Z. *Frontiers in Microbiology* **2016**, *7*, 1–7.
- (128) Douglas, T.; Young, M. *Science* **2006**, *312*, 873–875.
- (129) Mateu, M. G. *Protein Engineering, Design and Selection* **2011**, *24*, 53–63.
- (130) Pokorski, J. K.; Steinmetz, N. F. *Molecular Pharmaceutics* **2011**, *8*, 29–43.
- (131) Harada, L. K.; Silva, E. C.; Campos, W. F.; Del Fiol, F. S.; Vila, M.; Dabrowska, K.; Krylov, V. N.; Balcão, V. M. *Microbiological Research* **2018**, *212-213*, 38–58.
- (132) Pande, J.; Szewczyk, M. M.; Grover, A. K. *Biotechnology Advances* **2010**, *28*, 849–858.
- (133) Rami, A.; Behdani, M.; Yardehnavi, N.; Habibi-Anbouhi, M.; Kazemi-Lomedasht, F. *Asian Pacific Journal of Tropical Biomedicine* **2017**, *7*, 599–602.
- (134) Henry, K. A.; Arbabi-Ghahroudi, M.; Scott, J. K. *Frontiers in Microbiology* **2015**, *6*, 755.
- (135) Ong, H. K.; Tan, W. S.; Ho, K. L. *PeerJ* **2017**, *2017*, 1–31.
- (136) Dang, X.; Yi, H.; Ham, M. H.; Qi, J.; Yun, D. S.; Ladewski, R.; Strano, M. S.; Hammond, P. T.; Belcher, A. M. *Nature Nanotechnology* **2011**, *6*, 377–384.

- (137) Seo, Y.; Manivannan, S.; Kang, I.; Lee, S.-W.; Kim, K. *Biosensors and Bioelectronics* **2017**, *94*, 87–93.
- (138) Liu, S.; Zheng, C.; Ye, Z.; Blanc, B.; Zhi, X.; Shi, L.; Zhang, Z. *Macromolecules* **2018**, *51*, 8013–8026.
- (139) Röder, J.; Dickmeis, C.; Commandeur, U. *Frontiers in Plant Science* **2019**, *10*, 1–17.
- (140) Smartt, A. E.; Ripp, S. *Analytical and Bioanalytical Chemistry* **2011**, *400*, 991–1007.
- (141) Pires, D. P.; Cleto, S.; Sillankorva, S.; Azeredo, J.; Lu, T. K. *Microbiology and Molecular Biology Reviews* **2016**, *80*, 523–543.
- (142) Peng, H.; Chen, I. A. *ACS Nano* **2019**, *13*, 1244–1252.
- (143) Xiao, Y.; Isaacs, S. N. *Journal of Immunological Methods* **2013**, *384*, 148–151.
- (144) Wetzel, H. N.; Cohen, C.; Norman, A. B.; Webster, R. P. *Journal of Immunological Methods* **2017**, *448*, 80–84.
- (145) Linares, E. M.; Kubota, L. T.; Michaelis, J.; Thalhammer, S. *Journal of Immunological Methods* **2012**, *375*, 264–270.
- (146) Bahadır, E. B.; Sezgintürk, M. K. *Trends in Analytical Chemistry* **2016**, *82*, 286–306.
- (147) Adhikari, M.; Dhamane, S.; Hagström, A. E. V.; Garvey, G.; Chen, W.-H.; Kourentzi, K.; Strych, U.; Willson, R. C. *The Analyst* **2013**, *138*, 5584.

- (148) Adhikari, M.; Strych, U.; Kim, J.; Goux, H.; Dhamane, S.; Poongavanam, M. V.; Hagström, A. E.; Kourentzi, K.; Conrad, J. C.; Willson, R. C. *Analytical Chemistry* **2015**, *87*, 11660–11665.
- (149) Hagström, A. E.; Garvey, G.; Paterson, A. S.; Dhamane, S.; Adhikari, M.; Estes, M. K.; Strych, U.; Kourentzi, K.; Atmar, R. L.; Willson, R. C. *PLoS ONE* **2015**, *10*, 1–12.
- (150) Cox, C. R.; Jensen, K. R.; Mondesire, R. R.; Voorhees, K. J. *Journal of Microbiological Methods* **2015**, *118*, 51–56.
- (151) Li, Y.; Xie, G.; Qiu, J.; Zhou, D.; Gou, D.; Tao, Y.; Li, Y.; Chen, H. *Sensors and Actuators B: Chemical* **2018**, *258*, 803–812.
- (152) Wei, S.; Chelliah, R.; Rubab, M.; Oh, D. H.; Uddin, M. J.; Ahn, J. *Microorganisms* **2019**, *7*, 1–22.
- (153) Kim, H. J.; Ahn, K. C.; González-Techera, A.; González-Sapienza, G. G.; Gee, S. J.; Hammock, B. D. *Analytical Biochemistry* **2009**, *386*, 45–52.
- (154) Kim, H. J.; Rossotti, M. A.; Ahn, K. C.; González-Sapienza, G. G.; Gee, S. J.; Musker, R.; Hammock, B. D. *Analytical Biochemistry* **2010**, *401*, 38–46.
- (155) Kim, H. J.; McCoy, M.; Gee, S. J.; González-Sapienza, G. G.; Hammock, B. D. *Analytical Chemistry* **2011**, *83*, 246–253.
- (156) Zhang, H.; Xu, Y.; Huang, Q.; Yi, C.; Xiao, T.; Li, Q. *Chemical Communications* **2013**, *49*, 3778–3780.
- (157) Brasino, M.; Lee, J. H.; Cha, J. N. *Analytical Biochemistry* **2015**, *470*, 7–13.

- (158) Litvinov, J.; Hagström, A. E.; Lopez, Y.; Adhikari, M.; Kourentzi, K.; Strych, U.; Monzon, F. A.; Foster, W.; Cagle, P. T.; Willson, R. C. *Biotechnology Letters* **2014**, *36*, 1863–1868.
- (159) Kim, J.; Poling-Skutvik, R.; Trabuco, J. R. C.; Kourentzi, K.; Willson, R. C.; Conrad, J. C. *The Analyst* **2017**, *142*, 55–64.
- (160) Kim, J.; Vu, B.; Kourentzi, K.; Willson, R. C.; Conrad, J. C. *ACS Applied Materials and Interfaces* **2017**, *9*, 6878–6884.
- (161) Wang, J.; Yang, Y.; Yu, M.; Hu, G.; Gan, Y.; Gao, H.; Shi, X. *Journal of the Mechanics and Physics of Solids* **2018**, *112*, 431–457.
- (162) Mitchell, C. A.; Bahr, J. L.; Arepalli, S.; Tour, J. M.; Krishnamoorti, R. *Macromolecules* **2002**, *35*, 8825–8830.
- (163) Ferrier, R. C.; Lee, H.-S.; Hore, M. J. A.; Caporizzo, M.; Eckmann, D. M.; Composto, R. J. *Langmuir* **2014**, *30*, 1906–1914.
- (164) Meyer, R. A.; Green, J. J. *Wiley Interdiscip. Rev. Nanomed. Nanobiotechnol.* **2016**, *8*, 191–207.
- (165) Molaei, M.; Atefi, E.; Crocker, J. C. *Phys. Rev. Lett.* **2018**, *120*, 118002.
- (166) Ye, X.; Tong, P.; Fetters, L. J. *Macromolecules* **1998**, *31*, 5785–5793.
- (167) Tsay, J. M.; Doose, S.; Weiss, S. *J. Am. Chem. Soc.* **2006**, *128*, 1639–1647.
- (168) Broersma, S. *J. Chem. Phys.* **1960**, *32*, 1632–1635.
- (169) Broersma, S. *J. Chem. Phys.* **1960**, *32*, 1626–1631.
- (170) Tirado, M. M.; de la Torre, J. G. *J. Chem. Phys.* **1980**, *73*, 1986–1993.

- (171) Vasanthi, R.; Bhattacharyya, S.; Bagchi, B. *J. Chem. Phys.* **2002**, *116*, 1092–1096.
- (172) Alam, S.; Mukhopadhyay, A. *Macromolecules* **2014**, *47*, 6919–6924.
- (173) Choi, J.; Cargnello, M.; Murray, C. B.; Clarke, N.; Winey, K. I.; Composto, R. J. *ACS Macro Lett.* **2015**, *4*, 952–956.
- (174) Karatrantos, A.; Composto, R. J.; Winey, K. I.; Clarke, N. *Macromolecules* **2019**, *52*, 2513–2520.
- (175) Kim, J.; Adhikari, M.; Dhamane, S.; Hagstrom, A. E. V.; Kourentzi, K.; Strych, U.; Willson, R. C.; Conrad, J. C. *ACS Applied Materials and Interfaces* **2015**, *7*, 2891–2898.
- (176) De la Torre, J. G.; Martinez, M. C. L.; Tirado, M. M. *Biopolymers* **1984**, *23*, 611–615.
- (177) Barry, E.; Beller, D.; Dogic, Z. *Soft Matter* **2009**, *5*, 2563–2570.
- (178) Dogic, Z.; Fraden, S. *Phys. Rev. Lett.* **1997**, *78*, 2417–2420.
- (179) Kalnciema, I.; Balke, I.; Skrastina, D.; Ose, V.; Zeltins, A. *Mol. Biotechnol.* **2015**, *57*, 982–992.
- (180) Crocker, J. C.; Grier, D. G. *J. Colloid Interface Sci.* **1996**, *179*, 298–310.
- (181) Newman, J.; Swinney, H. L.; Day, L. A. *J. Mol. Biol.* **1977**, *116*, 593–603.
- (182) Maeda, T.; Fujime, S. *Macromolecules* **1985**, *18*, 2430–2437.
- (183) Lettinga, M. P.; Barry, E.; Dogic, Z. *Europhys. Lett.* **2005**, *71*, 692–698.

- (184) Yu, M.; Wang, J.; Yang, Y.; Zhu, C.; Su, Q.; Guo, S.; Sun, J.; Gan, Y.; Shi, X.; Gao, H. *Nano Lett.* **2016**, *16*, 7176–7182.
- (185) Lee, J.; Grein-Iankovski, A.; Narayanan, S.; Leheny, R. L. *Macromolecules* **2017**, *50*, 406–415.
- (186) Wang, B.; Anthony, S. M.; Bae, S. C.; Granick, S. *Proc. Natl. Acad. Sci. U. S. A.* **2009**, *106*, 15160–15164.
- (187) Chakrabarty, A.; Wang, F.; Sun, K.; Wei, Q. H. *Soft Matter* **2016**, *12*, 4318–4323.
- (188) Koens, L.; Lisicki, M.; Lauga, E. *Soft Matter* **2017**, *13*, 2977–2982.
- (189) Guan, J.; Wang, B.; Granick, S. *ACS Nano* **2014**, *8*, 3331–3336.
- (190) Jee, A.-Y.; Curtis-Fisk, J. L.; Granick, S. *Macromolecules* **2014**, *47*, 5793–5797.
- (191) He, W.; Song, H.; Su, Y.; Geng, L.; Ackerson, B. J.; Peng, H. B.; Tong, P. *Nat. Commun.* **2016**, *7*, 11701.
- (192) Lampo, T. J.; Stylianidou, S.; Backlund, M. P.; Wiggins, P. A.; Spakowitz, A. J. *Biophys. J.* **2017**, *112*, 532–542.
- (193) Slim, A. H.; Poling-Skutvik, R.; Conrad, J. C. *Langmuir* **2020**, *36*, 9153–9159.
- (194) Wong, I. Y.; Gardel, M. L.; Reichman, D. R.; Weeks, E. R.; Valentine, M. T.; Bausch, A. R.; Weitz, D. A. *Physical Review Letters* **2004**, *92*, 178101.
- (195) Guo, H.; Bourret, G.; Lennox, R. B.; Sutton, M.; Harden, J. L.; Leheny, R. L. *Physical Review Letters* **2012**, *109*, 055901.

- (196) Xue, C.; Zheng, X.; Chen, K.; Tian, Y.; Hu, G. *Journal of Physical Chemistry Letters* **2016**, *7*, 514–519.
- (197) Kohli, I.; Mukhopadhyay, A. *Macromolecules* **2012**, *45*, 6143–6149.
- (198) Poling-Skutvik, R.; Krishnamoorti, R.; Conrad, J. C. *ACS Macro Lett.* **2015**, *4*, 1169–1173.
- (199) Doi, M.; Edwards, S. F., *The Theory of Polymer Dynamics*, illustrate; Oxford University Press: New York, 1988, p 391.
- (200) Fakhri, N.; MacKintosh, F. C.; Lounis, B.; Cognet, L.; Pasquali, M. *Science* **2010**, *330*, 1804–1807.
- (201) Nam, G.; Johner, A.; Lee, N. K. *Journal of Chemical Physics* **2010**, *133*, DOI: 10.1063/1.3457999.
- (202) Hölzer, A.; Sommerfeld, M. *Powder Technol.* **2008**, *184*, 361–365.
- (203) Loth, E. *Powder Technol.* **2008**, *182*, 342–353.
- (204) Mandø, M.; Rosendahl, L. *Powder Technol.* **2010**, *202*, 1–13.
- (205) Voth, G. A.; Soldati, A. *Annu. Rev. Fluid Mech.* **2017**, *49*, 249–276.
- (206) Iannolo, G.; Minenkova, O.; Petruzzelli, R.; Cesareni, G. *J. Mol. Biol.* **1995**, *248*, 835–844.
- (207) Wang, Y. A.; Yu, X.; Overman, S.; Tsuboi, M.; Thomas, G. J.; Egelman, E. H. *J. Mol. Biol.* **2006**, *361*, 209–215.
- (208) Sattar, S.; Bennett, N. J.; Wen, W. X.; Guthrie, J. M.; Blackwell, L. F.; Conway, J. F.; Rakonjac, J. *Frontiers in Microbiology* **2015**, *6*, 316.

- (209) Smith, D. E.; Perkins, T. T.; Chu, S. *Macromolecules* **1996**, *29*, 1372–1373.
- (210) Petrov, E. P.; Ohrt, T.; Winkler, R. .; Schwille, P. *Phys. Rev. Lett.* **2006**, *97*, 258101.
- (211) Prieto-Simón, B.; Noguer, T.; Campàs, M. *TrAC - Trends in Analytical Chemistry* **2007**, *26*, 689–702.
- (212) Maragos, C. M. *Analytical and Bioanalytical Chemistry* **2009**, *395*, 1205–1213.
- (213) Pastor-Navarro, N.; Maquieira, Á.; Puchades, R. *Analytical and Bioanalytical Chemistry* **2009**, *395*, 907–920.
- (214) Pikkemaat, M. G. *Analytical and Bioanalytical Chemistry* **2009**, *395*, 893–905.
- (215) Herman, J.; Shushan, B. In *Tandem Mass Spectrometry - Applications and Principles*, Prasain, J. K., Ed.; InTech: Rijeka, Croatia, 2012; Chapter 28, pp 673–720.
- (216) Matsuda, R.; Rodriguez, E.; Suresh, D.; Hage, D. S. *Bioanalysis* **2015**, *7*, 2947–2966.
- (217) Fintschenko, Y.; Wilson, G. S. *Microchimica Acta* **1998**, *129*, 7–18.
- (218) Pfaunmiller, E. L.; Anguizola, J. A.; Milanuk, M. L.; Carter, N.; Hage, D. S. *Journal of Chromatography B* **2016**, *1021*, 91–100.
- (219) Huttunen, R. J.; Näreoja, T.; Mariani, L.; Härmä, H. *Biosensors and Bioelectronics* **2016**, *83*, 54–59.

- (220) Liu, H.; Rong, P.; Jia, H.; Yang, J.; Dong, B.; Dong, Q.; Yang, C.; Hu, P.; Wang, W.; Liu, H.; Liu, D. *Theranostics* **2016**, *6*, 54–64.
- (221) Kim, D.; Kwon, H. J.; Shin, K.; Kim, J.; Yoo, R.-E.; Choi, S. H.; Soh, M.; Kang, T.; Han, S. I.; Hyeon, T. *ACS Nano* **2017**, *11*, 8448–8455.
- (222) Pyun, J.-C.; Jose, J.; Park, M. *Analyst* **2017**, *142*, 1720–1728.
- (223) Chen, H.; Hagström, A. E. V.; Kim, J.; Garvey, G.; Paterson, A.; Ruiz-Ruiz, F.; Raja, B.; Strych, U.; Rito-Palomares, M.; Kourentzi, K.; Conrad, J. C.; Atmar, R. L.; Willson, R. C. *Scientific Reports* **2016**, *6*, 24297.
- (224) Kallberg, K.; Johansson, H.-O.; Bulow, L. *Biotechnology Journal* **2012**, *7*, 1485–1495.
- (225) Ji, Y.; Tian, Y.; Ahnfelt, M.; Sui, L. *Journal of Chromatography A* **2014**, *1348*, 137–149.
- (226) Blom, H.; Åkerblom, A.; Kon, T.; Shaker, S.; van der Pol, L.; Lundgren, M. *Vaccine* **2014**, *32*, 3721–3724.
- (227) Healthcare, G. *Application Note* **2014**, *29*, 1–6.
- (228) Weigel, T.; Solomaier, T.; Peucker, A.; Pathapati, T.; Wolff, M. W.; Reichl, U. *Journal of Virological Methods* **2014**, *207*, 45–53.
- (229) James, K. T.; Cooney, B.; Agopsowicz, K.; Trevors, M. A.; Mohamed, A.; Stoltz, D.; Hitt, M.; Shmulevitz, M. *Scientific Reports* **2016**, *6*, 36826.
- (230) Tseng, Y.-F.; Weng, T.-C.; Lai, C.-C.; Chen, P.-L.; Lee, M.-S.; Hu, A. Y.-C. *Vaccine* **2018**, *36*, 3146–3152.

- (231) Mundle, S. T.; Kishko, M.; Groppo, R.; DiNapoli, J.; Hamberger, J.; McNeil, B.; Kleanthous, H.; Parrington, M.; Zhang, L.; Anderson, S. F. *Vaccine* **2016**, *34*, 3690–3696.
- (232) Zaveckas, M.; Goda, K.; Ziogiene, D.; Gedvilaite, A. *Journal of Chromatography B* **2018**, *1090*, 7–13.
- (233) Pato, T. P.; Souza, M. C. O.; Mattos, D. A.; Caride, E.; Ferreira, D. F.; Gaspar, L. P.; Freire, M. S.; Castilho, L. R. *Vaccine* **2019**, *37*, 3214–3220.
- (234) Pezzini, J.; Joucla, G.; Gantier, R.; Toueille, M.; Lomenech, A.-M.; Le Sénéchal, C.; Garbay, B.; Santarelli, X.; Cabanne, C. *Journal of Chromatography A* **2011**, *1218*, 8197–8208.
- (235) Mansour, F. R.; Danielson, N. D. *Analytical Methods* **2013**, *5*, 4955–4972.
- (236) Paul, J.; Jensen, S.; Dukart, A.; Cornelissen, G. *Journal of Chromatography A* **2014**, *1366*, 38–44.
- (237) Karkov, H. S.; Sejergaard, L.; Cramer, S. M. *Journal of Chromatography A* **2013**, *1318*, 149–155.
- (238) Sejergaard, L.; Karkov, H. S.; Krarup, J. K.; Hagel, A. B. B.; Cramer, S. M. *Biotechnology Progress* **2014**, *30*, 1057–1064.
- (239) Miller, M. D.; Benedik, M. J.; Sullivan, M. C.; Shipley, N. S.; Krause, K. L. *Journal of Molecular Biology* **1991**, *222*, 27–30.
- (240) Savory, J.; Pu, P. H.; Sunderman, F. W. *Clinical Chemistry* **1968**, *14*, 1160–1171.

- (241) Datta, P.; Meli, L.; Li, L.; Migliore, N.; Schaefer, E.; Sharfstein, S. T.; Dordick, J. S.; Linhardt, R. J. *Biotechnology Journal* **2014**, *9*, 386–395.
- (242) Lubran, M. M. *Annals of Clinical and Laboratory Science* **1978**, *8*, 106–110.
- (243) Healthcare, G. *Application Note* **2014**, *29*, 1–8.
- (244) *Engineering Applications of Nanotechnology: From Energy to Drug Delivery*; Korada, V. S., Hamid, N. H. B., Eds.; Springer: 2017.
- (245) Jawahar, N.; Meyyanathan, S. N. *International Journal of Health Allied Sciences* **2012**, *1*, 217.
- (246) Elahi, N.; Kamali, M.; Baghersad, M. H. *Talanta* **2018**, *184*, 537–556.
- (247) Lane, L. A.; Qian, X.; Smith, A. M.; Nie, S. *Annual Review of Physical Chemistry* **2015**, *66*, 521–547.
- (248) Kas, J.; Strey, H.; Tang, J. X.; Finger, D.; Ezzell, R.; Sackmann, E.; Janmey, P. A. *Biophysical Journal* **1996**, *70*, 609–625.
- (249) Nam, G.; Johner, A.; Lee, N. K. *European Physical Journal E* **2010**, *32*, 119–126.
- (250) Abadi, M.; Serag, M. F.; Habuchi, S. *Nature Communications* **2018**, *9*, 5098.
- (251) Brangwynne, C. P.; Koenderink, G. H.; Barry, E.; Dogic, Z.; MacKintosh, F. C.; Weitz, D. A. *Biophysical Journal* **2007**, *93*, 346–359.
- (252) Yi, M. K.; Villanueva, R. A.; Thomas, D. L.; Wakita, T.; Lemon, S. M. *Proceedings of the National Academy of Sciences of the United States of America* **2006**, *103*, 2310–2315.

- (253) Branston, S. D.; Stanley, E. C.; Ward, J. M.; Keshavarz-Moore, E. *Biotechnology and Bioprocess Engineering* **2013**, *18*, 560–566.
- (254) García, R.; Latz, S.; Romero, J.; Higuera, G.; García, K.; Bastías, R. *Frontiers in Microbiology* **2019**, *10*, 1187.
- (255) Marvin, D. A.; Hale, R. D.; Nave, C.; Citterich, M. H. *Journal of Molecular Biology* **1994**, *235*, 260–286.
- (256) Marinelli, L. J.; Hatfull, G. F.; Piuri, M. *Bacteriophage* **2012**, *2*, 5–14.
- (257) Badran, A. H.; Liu, D. R. *Nature Communications* **2015**, *6*, 1–10.
- (258) Davis, J. N.; van den Pol, A. N. *Journal of Virology* **2010**, *84*, 1625–1630.
- (259) Eiben, S.; Stitz, N.; Eber, F.; Wagner, J.; Atanasova, P.; Bill, J.; Wege, C.; Jeske, H. *Virus Research* **2014**, *180*, 92–96.
- (260) Held, H. A.; Sidhu, S. S. *Journal of Molecular Biology* **2004**, *340*, 587–597.
- (261) Tridgett, M.; Lloyd, J. R.; Kenne, J.; Moore-kelly, C.; Da, T. R. *Bioconjugate Chemistry* **2018**, *29*, 1872–1875.
- (262) Cate, D. M.; Adkins, J. A.; Mettakoonpitak, J.; Henry, C. S. *Analytical Chemistry* **2015**, *87*, 19–41.
- (263) Puig, H. D.; Bosch, I.; Carre, M.; Hamad-schi, K. *Bioconjugate Chemistry* **2017**, *28*, 230–238.
- (264) Gasperino, D.; Baughman, T.; Hsieh, H. V.; Bell, D.; Weigl, B. H. *Annual Review of Analytical Chemistry* **2018**, *11*, 219–244.

- (265) Kaufman, E.; Lamster, I. B. *Critical Reviews in Oral Biology Medicine* **2002**, *13*, 197–212.
- (266) Ryan, D.; Robards, K.; Prenzler, P. D.; Kendall, M. *Analytica Chimica Acta* **2011**, *684*, 17–29.
- (267) Martí-Álamo, S.; Mancheño-Franch, A.; Marzal-Gamarra, C.; Carlos-Fabuel, L. *Journal of Clinical and Experimental Dentistry* **2012**, *4*, e237–e243.
- (268) Yin, P.; Lehmann, R.; Xu, G. *Analytical and Bioanalytical Chemistry* **2015**, *407*, 4879–4892.
- (269) Jurowski, K.; Kochan, K.; Walczak, J.; Barańska, M.; Piekoszewski, W.; Buszewski, B. *Trends in Analytical Chemistry* **2017**, *86*, 276–289.
- (270) Capelli, L.; Taverna, G.; Bellini, A.; Eusebio, L.; Buffi, N.; Lazzeri, M.; Guazzoni, G.; Bozzini, G.; Seveso, M.; Mandressi, A.; Tidu, L.; Grizzi, F.; Sardella, P.; Latorre, G.; Hurle, R.; Lughezzani, G.; Casale, P.; Meregali, S.; Sironi, S. *Sensors* **2016**, *16*, 1708.
- (271) Tang, R.; Yang, H.; Choi, J. R.; Gong, Y.; Hu, J.; Feng, S.; Pingguan-Murphy, B.; Mei, Q.; Xu, F. *Talanta* **2016**, *152*, 269–276.
- (272) Mori, S.; Barth, H. G., *Size Exclusion Chromatography*, 1st ed.; Springer: Berlin, Heidelberg, 1999, p 234.
- (273) Kelley, B. *mAbs* **2009**, *1*, 443–452.
- (274) Wohlgemuth, R. In *Comprehensive Biotechnology*, Moo-Young, M., Ed., 2nd ed.; Elsevier B.V.: New York, 2011; Vol. 2; Chapter 2, pp 591–601.

- (275) Levy, N. E.; Valente, K. N.; Choe, L. H.; Lee, K. H.; Lenhoff, A. M. *Biotechnology and Bioengineering* **2014**, *111*, 904–912.
- (276) Patel, B. A.; Pinto, N. D.; Gospodarek, A.; Kilgore, B.; Goswami, K.; Napoli, W. N.; Desai, J.; Heo, J. H.; Panzera, D.; Pollard, D.; Richardson, D.; Brower, M.; Richardson, D. D. *Analytical Chemistry* **2017**, *89*, 11357–11365.